
Paper:

Liu, G., Winwood, S., Rhodes, K. & Birosca, S. (2019). The effects of grain size, dendritic structure and crystallographic orientation on fatigue crack propagation in IN713C nickel-based superalloy. *International Journal of Plasticity*

http://dx.doi.org/10.1016/j.ijplas.2019.09.010

The Effects of Grain Size, Dendritic Structure and Crystallographic Orientation on Fatigue Crack Propagation in IN713C Nickel-Based Superalloy

Gang Liu[1*], Sean Winwood[2], Katie Rhodes[2], Soran Birosca[1*]

[1] Materials Research Centre, College of Engineering, Swansea University, Bay Campus, Swansea SA1 8EN, UK.

[2] Cummins Turbo Technologies, St. Andrews Rd., Huddersfield HD1 6RA, UK.

Abstract

The polycrystalline IN713C produced via investment casting is one of the widely-used nickel-based superalloy in automotive and aerospace industries. This alloy, however, has an apparent inhomogeneous microstructure generated during casting and contains dendritic structure that gives rise to strain localisation during loading. Yet, the effect of dendritic structure, grain size and shape as well as crystallographic orientation, which directly influence fatigue property and deformation micromechanism in the components, is rarely studied. In the present study, IN713C cast bars are tailored with three different grain structures, i.e., transition, equiaxed and columnar, with substantial grain size variations. The produced bars were tested under strain controlled LCF (Low Cycle Fatigue) and stress controlled HCF (High Cycle Fatigue) conditions at 650 °C. The results showed that most of fatigue cracks initiated from casting pores and fatigue life extended in the microstructure with a small grain size during both HCF and LCF loadings. It is also demonstrated that fatigue striations were mainly observed within dendritic areas during crack propagation, whereas the higher GND (Geometrically Necessary Dislocation) density were predominantly observed in the interdendritic areas. Here, we propose a concept of ‘Crack Propagation Unit (CPU)’ for better description of deformation mechanism at local scale during fatigue loading by combining fracture surface characteristic methodology and dislocation distribution analyses within the dendritic structural unit. Furthermore, this model to understand the deformation micromechanism can provide a new perspective on the interpretation of Hall-Petch relationship in casting materials that contain dendritic structure. This is further demonstrated via direct correlation of the high crack propagation resistance with the crack path divergence instead of the dislocation pile-up at the grain boundary or in-between the γ/ γ’ channels. Moreover, by utilising serial sectioning method followed by layered EBSD scanning, quasi-3-D grain orientation mappings were obtained, and crystallographic texture information were directly correlated with the fracture surface observations. This allowed an investigation of the influence of orientation of individual grains and micro/macro texture on crack propagation rate. The critical stage of crack propagation in fatigue life and its correlations with microstructural features is established, offering potential practical applications by controlling the investment casting process parameters.

Key words: Nickel-based Superalloy; Fatigue Crack propagation; Dendritic structure; Grain size; Microtexture; GND.

* To whom correspondence should be addressed:

Gang.Liu@swansea.ac.uk (G. Liu); S.Birosca@swansea.ac.uk (S. Birosca)

1. Introduction

Directionally cast nickel-based superalloy generally exhibits high strength at elevated temperatures due to their possession of higher volume fraction of strengthening phase of γ’ (up to 70%) (Reed, 2008; Pollock and Tin, 2006). Moreover, superalloy produced via investment casting also has the advantage of minimising machining process compared to the forged alloys, which is of significant economic efficiency and enable massive industrial production. IN713C has been widely used as turbocharger turbine wheel materials in the automotive industry for decades (Salvat Cantó et al., 2018; Liu et al., 2018). However, casting has an inherent problem of porosity formation (shrinkage and/or gas pore) and usually results in relatively large grains, which degrades the alloy's fatigue property to a great degree. The fatigue failure is counted for 90% of the total component failures used in critical applications, thus both LCF and HCF in superalloys have received considerable academic and industrial interests (Huang et al., 2010). The general concepts and theories of fatigue developed from other metals also have been successfully applied to newly developed superalloys. Although from the fracture mechanics point of view, the crack propagation is the fatigue determining step, especially for the alloys used in high temperature applications, however, still more academic research attentions are paid on crack initiation stage (Chan, 2010; Pineau et al., 2016). Those studies mainly focused on slip bands formation (Dunne et al., 2007), pores, inclusions (Jiang et al., 2016; Chen et al., 2018) or special grain boundary characteristics (Miao et al., 2009; Stinville et al., 2018). Indeed, the crack nucleation stage covers large portion of the total fatigue life, particularly in HCF regime where the alloy is subjected to low applied stresses. Moreover, it is well established that the crack initiation threshold is directly related to the presence of the defects such as pores, pre-existing cracks and inclusions. However, with the technological advancements in the alloys processing routes, these defects that act as local stress concentration sites, are largely minimised which can delay crack initiation greatly (Chan, 2010). Nonetheless, defects cannot be eliminated completely even using most advanced processing methods including powder metallurgy, thus stress concentration points and crack initiation sites are always available. Therefore, fatigue life should be controlled in crack propagation stage via designing an optimum microstructure for crack growth resistance.

The lack of 3-D and non-destructive crack observation in most of the studies in the literature added further difficulty in correlating crack path interaction with individual microstructure features. For instance, fatigue striation, a unique indicative feature in fatigue propagation process that is able to provide detailed information about deformation mechanism, can only be observed and analysed after complete fracture. Although striation usually is used as indication of fatigue process occurrence and sometimes quantitatively correlated with propagation rate (Riemelmoser et al., 1998; Shao et al., 2017), very few reports have investigated the distribution of striations and their interaction with local microstructures, which is critical in understanding the effects of microstructure on crack propagation process. In general, multi-phenomena occurs during alloy casting, including element partitioning, dendrite formation and second phase precipitation, leading to overall heterogeneous microstructure. This produced microstructure in the solidified alloy allows strain localisation during fatigue loading (Coleman et al., 2016). The authors of this study believe that in order to obtain complete description of deformation mechanism during fatigue crack propagation stage in cast materials, the effects of dendritic structure, grain size and microtexture should be thoroughly addressed.

The pioneering work on possible effects of dendritic structure on fatigue life was conducted by Horstemeyer et al. (2004) on a die cast magnesium alloy. They demonstrated that the HCF life might be affected by average secondary dendrite arm spacing in addition to the drastic difference in nucleation site size and average grain size. In our earlier work (Liu et al., 2018) we proposed a strain accommodation model via lattice rotation of interdendritic area in the late stage of crack propagation in IN713C superalloy. However, the question of to what extend the dendritic structure affects crack propagation and overall deformation mechanism remained unanswered.

The effect of grain size on mechanical properties and in particular on fatigue crack growth is studied extensively (Krupp, 2007; Thompson and Backofen, 1971; Duber et al., 2006) The classical empirical Hall-Patch relationship which implies the benefit of small grain size in increasing material strength, has been successfully applied to many metals/alloys. The classical explanation for this relationship is either dislocation pile-up at grain boundaries that act as crack barriers in small size grains or large local stress generation by dislocation accumulation leading to easy slip activation in the neighbouring large grains (Krupp, 2007). Many recent researches on slip transmission (Zheng et al., 2017; Grilli et al., 2018) or dislocation transmission (Ding et al., 2016) across grain boundary confirmed and further developed this theory. Furthermore, gradient grain size structure has been developed and showed enhanced fatigue crack growth resistance (Shao et al., 2017). Nevertheless, Hall-Patch relationship usually apply to homogeneous single-phase materials. In the current investigation, we examine to what extent this relationship can be valid in heterogeneous multi-phase system such as in solidified IN713C superalloy, and how dislocation accumulation and behaviour can govern Hall-Patch relationship and overall deformation micromechanism during LCF and HCF Loading.

The individual grain crystallographic orientation, microtexture, macrotexture and mesotexture are also significant parameters in determining crack initiation sites as well as crack propagation path. Moreover, it is well established that both grain boundary's tilt and twist misorientation angles should be considered in crack growth investigation (Zhai et al., 2000). This is due to the significant role of grain boundaries that act as a barrier to slip or crack transfers. However, recognising the grain boundary plane, which is critical for complete grain boundary characterisations, is not straightforward without obtaining 3-D information. Thus, obtaining micro/meso-texture information in 3-D is important to observe the crack path. One difficulty of such study is to provide such 3-D vision of orientation distribution. Amongst destructive and post-mortem way for fatigue research, serial sectioning method can give 3-D information either by focussed ion beam (FIB) milling (Zaefferer et al., 2008) or mechanical serial polishing (Pirgazi et al., 2014), from which 3-D images of short cracks can be reconstructed. It is important to correlate the microstructure/texture to the crack path in 3-D, as fatigue striations are essentially formed by the alternating slip activation and blunting on different slip systems which depend on crystallographic orientations (Bowles and Broek, 1972; Cai and McEvily, 2001). By combining diffraction and phase-contrast X-ray tomography technique, Herbig et al. (Herbig et al., 2011) made the first attempt to correlate fracture surface, grain orientation and propagation rate in 3-D in an in-situ and non-destructive way.

The mechanical behaviour and dislocation substructure of IN713C or IN713LC alloy subjected to cyclic loading have been reported (Petrenec et al., 2005; Gelmedin et al., 2010; Kunz et al., 2010). For instance, Petrenec et al. (2005) observed plannar dislocation arrangements in the form of bands parallel to the {111} planes in IN713C cycled in temperature between 300-1073 K. However, very few researches have correlated the dislocation density/distribution to the fatigue process, fracture surface and critical microstructures such as dendritic structure. Thus, a comprehensive understanding of deformation micromechanism in this alloy is needed.

The background of this research is to establish an exact relationship between fatigue property and microstructure/microtexture in IN713C nickel-based superalloy used for turbocharger turbine blade at elevated temperature. The turbine blade produced via investment casting consists of two distinctive grain size structures across the component. In the current study, standard fatigue test bars have been produced with different grain structures and standard LCF and HCF tests have been conducted in a controlled way. In addition to crack initiation stage, this investigation mainly focused on crack propagation stage and its relationship with local microstructural features such as dendritic structure, grain size and micro/macro/meso-texture, to portray exact deformation mechanism in IN713C nickel-based superalloy.

2. Materials and experiment procedures

2.1 Bars produced by investment casting

The materials used in this study was IN713C nickel-based superalloy with the chemical composition shown in Table 1. As described in Section 1, during investment casting of turbocharger turbine blades, the complex geometrical configuration leads to different cooling rates in different areas, resulting in disparity of grain structure across the blade, i.e., large columnar grain area, fine equiaxed grains at the tip of blades and transition area between the two (Salvat Cantó et al., 2018; Coleman et al., 2016). In order to study the effects of all three grain structures on fatigue property, three different microstructures of columnar, equiaxed and transition bars were produced via investment casting at Cummins Turbo Technologies at Huddersfield, UK. The initial LCF property of these bars was recently reported in (Salvat Cantó et al., 2018). The detailed manufacturing process for the bars can be found in (Salvat Cantó et al., 2018). The produced bars of the three distinctive microstructures, i.e., transition, equiaxed and columnar, are shown in Fig. 1a. The EBSD orientation mapping were conducted on the bar area indicated in Fig. 1b and shown in Figs. 1c, 1d, 1e for Transition (T), Equiaxed (E) and Columnar (C), respectively. For transition bar, the average grain size transit from ~ 635 μm (upper part in Fig. 1c) to ~ 2145 μm (lower part in Fig. 1c), while for equiaxed and columnar samples, the average grain size are ~ 1745 μm (Fig. 1d, f) and ~ 2960 μm (Fig. 1e, f), respectively. The IPFs (Inverse Pole Figures, Fig. 1c-e) show no strong texture in any of the bars. A typical microstructure that exist in all three bars consisted of dendritic structure (Fig. 2a), MC-type carbides mainly distributed within interdendritic area (Fig. 2b) and precipitate strengthening phase γ' in both dendritic area (Fig. 2c) and interdendritic area (Fig. 2d) with average size of ~ 500 nm. It should be noted here that all three bars show no significant variation in dendrite, carbides and γ' shape, size and morphologies.

2.2 Low and high cycle fatigue tests

A set of cylindrical fatigue test specimens with geometry are shown in Fig. 3a. Fatigue test specimen with gauge length of 18 mm and gauge diameter of 6 mm were machined from as-received bars. Before test, the samples were low-stress ground & longitudinally polished to a surface finish of < 0.2 μm. The LCF tests were conducted according to ASTM E606 standards and under strain control with maximum strain of 0.4%. The maximum stress in LCF was reached ~630, ~660 and ~670 MPa for Transition, Equiaxed and Columnar structure, respectively. Stress amplitudes and some selected stress-strain loop in LCF tests are shown in Supplementary Fig. 1. The HCF tests were conducted according to ASTM E466 standards and under stress control. The maximum stress values were obtained by tensioning the samples up to 0.2% strain and was ~335, ~345, ~329 MPa for Transition, Equiaxed and Columnar structure, respectively. The test frequency for LCF and HCF were 0.5 Hz and 30 Hz, respectively. Both LCF and HCF tests were conducted at the R-ratio of -1, with sinusoidal waveform and at 650 °C.

2.3 Microstructure and microtexture characterisations

Following the fatigue tests, the fracture surfaces of failed sample were cleaned by ultrasonic bathing in detergent solution for 20 minutes and then in ethanol for another 20 minutes. Fractography observations were then carried out using Keyence light microscope and Scanning Electron Microscope (SEM), using Zeiss (EVO) and JEOL 7800F Field Emission Gun (FEG) microscopes. After complete fracture surface characterisation, serial sectioning of the failed fatigue samples along Loading Direction (LD) were performed in order to correlate the fracture surface with microstructure and microtexture beneath the fracture surface in three dimensions (3-D). A schematic graph in Fig. 3b shows the sectioning process with only two cross sectioning (CS) planes (CS 1 and CS 2) displayed. The 3-D sectioning procedures were as follows: The first flat plane along LD was made by carefully grinding the cylindrical sample to nearly parallel to the central crack growth direction from initiation sites with the help of optical microscope during grinding process. Then the sample was mounted with conductive bakelite and the flat surface was further polished and culminated with 0.05 μm colloidal silica for 10 min, followed by EBSD scanning. After first layer characterisation (microstructure and EBSD mapping), the sample was further grinded and polished by removing 300~500 μm in depth according to the average grain size of the cast specimen followed by another EBSD scanning. This subsequent layer-by-layer 'grinding-polishing-EBSD scanning' was carried out with the sample dismounted in between every two sections for SEM observation to align the fracture surface with the EBSD scanned planes. In the meantime, following each EBSD scan, the mounted sample was electrolytically etched using 10% phosphoric acid at 3-5V for 3-5s to characterise γ’, carbides and oxides as well as imaging secondary cracks.

High resolution imaging and EBSD mapping were performed using JEOL 7800F FEG-SEM equipped with AZTEC data acquisition and analysis software with a Nordlys EBSD detector. The SEM operating voltage used was 10-20 kV for imaging and 20 kV for EBSD scan with a current of ~ 14nA. For layer-by-layer and large EBSD mapping, a binning of 8×8 and step size of 8 μm were used to balance the scanning time and quality required. Whilst for high resolution EBSD (HR-EBSD) scanning used for GND calculation, a binning of 4×4 and step size of 100 nm were selected, with an exposure time of 150 ms per pattern. The EBSD data analysis was conducted using standard HKL-EBSD Channel 5 software package. The GND and slip trace mapping were calculated using in-house python code. The principles and details of the calculations were reported previously in (Liu et al., 2018; Birosca et al., 2014, 2019). Furthermore, specific site extraction close to initiation sites and beneath fatigue striations for the dislocation analyses were prepared using Focus Ion Beam (FIB) and characterised by means of FEI-Talos 200F utilising Scanning Transmission Electron Microscopy (STEM)-High Angle Annular Dark field (HAADF). Further TEM specimens close to initiation sites were cut out as thin plate along LD and then grinded and polished to ~100 μm in thickness. After punching into 3 mm diameter foils, they were further polished to ~50 μm, followed by twin-jet electronic polishing using Struers Tenupol III. For this, an electrolyte of 10% perchloric acid in methanol was used at -20 ºC and 20 V.

3. Results

3.1 General description of crack initiation and propagation during LCF and HCF.

3.1.1 Fatigue life and overview of fracture surface

The middle cross-section microstructure beneath the fracture surface for the LCF and HCF tested samples are shown in Fig. 3. The fracture surface of each tested sample together with fatigue life for

LCF and HCF are shown in Fig. 4 and Supplementary Fig. 2 (SEM images). The grain size mapping and average grain size of tested sample are also shown in Supplementary Fig. 2. Figs. 3c-h shows EBSD-derived IPF // LD maps, revealing the grain size, shape and orientation in the cross-section plane that is indicated by the red dashed line on each sample in Figs. 4a-c and 4e-g. Given the relatively uniform grain size distribution in Equiaxed (E) and Columnar (C) grain structures, only half of the failed samples (bottom half) were prepared for EBSD mapping. However, for Transition (T) structure, both halves of the fractured samples were mapped to identify possible transition area, see Figs. 3c and 3f. From Fig. 3, it is clear that the columnar microstructure exhibited largest grain sizes among the three produced microstructures. However, the grain size in equiaxed bar tested under HCF condition (Fig. 3g), is significantly smaller than that of equiaxed bar tested under LCF condition in Fig. 3d. Thus, there are some grain size disparities in the bars. However, the main purpose of achieving small equiaxed grains to be compared to a large columnar microstructure was produced from the investment casting trails. Moreover, transition area could not be found around failed area in transition samples. This is not unexpected as producing transition area in the exact centre of the cast bar is very difficult. Also, there is some discrepancy in the grain sizes in bars of transition microstructure, see Figs. 3c and 3f. Thus, the produced transition bars cannot be representative of actual transition microstructure in turbine wheel blades. Therefore, due to the inconsistency between the actual produced microstructures and expected grain sizes, the present study will focus on the effects of grain size in individual bars on fatigue properties. However, here we use the initial notation of originally designated microstructure for simplicity, e.g., T stands for Transition structure (although transition area was not observed in the middle of the specimen). L and H notations are used for the samples tested in Low and High cycle fatigues, respectively. For example, L-T, L-E and L-C stand for LCF-Transition, LCF-Equiaxed and LCF-Columnar, respectively, see Fig. 4.

Nearly all the samples failed from subsurface casting pores during both LCF and HCF tests. In general, the fatigue failure process during both LCF and HCF conditions consists of three distinctive stages: crack initiation (mainly from casting pore), propagation and overload regime. The prominent feature of crack initiation stage during HCF at relatively low temperature (below 800-850°C) is the 'facet' formation (Fig. 4e-g), which is due to crack initiation at stress concentrators and subsequent propagation along {111} planes (Pollock and Tin, 2006; Krupp, 2007). The crack propagation stage is characterised as a relatively flat surface and fatigue striations which will be quantitatively analysed in detail in following sections. The overload (final rupture) regime, however, features rough fracture surface and visible dendritic structures, see the primary dendritic arms within the overload areas in Fig. 4b. It should be emphasised here that the colour contrast in optical images is very useful in distinguishing all three crack stages. The crack propagation areas are usually covered by shinny dark blue colour due to oxidation occurrence at 650°C, whereas the overload areas by yellow or whitish colours. The white dashed lines in Fig. 4 are used to separate the propagation area from the overload area. The exception is L-C sample where there are 2 white dashed lines as there is a 'mixed area' between the lines consisting of both crack propagation and overload features.

It is evident from Figs. 4d and 4h that in both LCF and HCF, longer fatigue lives benefit from smaller grain size. For instance, the fatigue life of L-T sample with ~510 μm average grain size is four times greater (4694 cycles) than in L-E sample (1147 cycles) with ~1150 μm grain size, and double life times than in L-C sample (1981cycles) with ~ 1030 μm grain size, see Figs. 4d and Supplementary Fig. 2e. Similarly, during HCF, small grain sample (H-E) has much higher fatigue cycles than large grain samples (H-T and H-C), see Fig. 4h. The crack propagation length, which is defined and measured from initiation site to the division line between propagation and overload areas (i.e., the white dashed line in Fig. 4), is indicated by the yellow dashed double arrows on the same figures. It shows that the higher fatigue life in small grain samples is partially resulted from longer fatigue crack propagation stage, in addition to smaller pore size in small grain samples that can contribute to greater fatigue life (Horstemeyer et al., 2004). The relationship between grain size and crack propagation rate will be further discussed in Section 4.

It should be mentioned here that according to the selected cyclic stress-strain response in LCF tests (Supplementary Fig. 1b and 1c), the plastic strain amplitude was negligible compared to the total strain (0.4%), i.e., most of the deformation was microscopically under elastic regime fatigue loading. Therefore, the deformation process would be mainly determined by the local plasticity and local heterogeneous structures. The selection of total strain of 0.4% in the current study was based on our previous investigation results on IN713C under the same loading conditions (Salvat Cantó et al., 2018).

3.1.2 Crack initiation and propagation stage

The Supplementary Fig. 3 shows an example of the effect of porosity on crack initiation stage in H-C sample. In Supplementary Fig. 3a, the EBSD-IPF maps are superimposed on SEM images of the same areas observed. The results suggest that most of pores formed on the grain boundary junction. Moreover, Supplementary Fig. 3c shows a high GND density around the pore where the crack is initiated. This demonstrates the dislocation evolution and accumulation during the crack nucleation period, and consistent with the modelling result by Dezecot et al. (2017).

A general observation of crack propagation process is shown macroscopically in Fig. 5a-c and microscopically in Fig. 5d-k for L-E sample. The major propagation areas are roughly divided into low and high propagation rate regimes according to the spacing of striations. The area between microstructurally crack propagation and overload areas, which is called a transition or 'mixed area' are also schematically shown in Fig. 5a. This transition area is characterised with a mixed striation (common feature in propagation area) and rough dendritic structure (common feature in overload area). It is generally believed that fatigue striation is the most distinguishable feature in fatigue crack propagation on fracture surface. Here, we assume that the striations were produced based on cycle-by-cycle mode and determine the crack propagation rate by measuring the average spacing between the adjacent striations. This assumption has been previously verified for wide stress amplitudes (Riemelmoser et al., 1998) and in very low stress amplitude (Cai and McEyily, 2001). In this example, the propagation rate increased from ~ 0.2 μm / cycle in low propagation rate regime to 0.8 μm / cycle in the high propagation rate regime and 1.8 µm / cycle in the transition area, see Fig. 5e and Fig. 5f, respectively. Moreover, it is interesting to see the distorted γ' beneath the fracture surface in different crack propagation stage areas, see Fig.5h-k, which reflect the loading history and stress state during fatigue test. Moreover, shallow oxide scales with thickness of ~200 nm (Fig. 5h) to ~150 nm (Fig. 5j) was observed on the samples' cross-section due to air exposure during fatigue tests, see the double red dashed lines in Figs. 5h-j.

3.2 Fatigue striation and GND local accumulations

3.2.1 Fatigue striation within dendritic structure

A notable relationship between striation distribution and dendritic structure was observed. It is established that the fatigue striation was only limited in dendritic core areas (including both primary dendritic and secondary dendritic areas) in both LCF and HCF. Fig. 6 shows three examples of striations within secondary dendritic areas: Fig. 6a-d, 6e-h and 6i obtained from sample L-C, H-E and L-T, respectively. The optical images (Figs. 6a, 6e, 6i) show that the fracture surface in propagation areas were covered by blue intermittent small blocky shape regions with narrow brownish channels in between. On a macroscale level, these individual blocky areas present a wave-like shape along crack propagation direction, see in Figs. 6e and 6f (which are the same area). The brownish and bluish parts however, are the interdendritic and secondary dendritic areas, respectively, see Fig. 6i. This can be further confirmed by measuring the size of blue area in SEM image (Fig. 6b) and dendrite arm size in polished optical image (Fig. 6d), which shows the equivalent dimensions in both imaging modes (~70 µm in width and 100-200 µm in length). Moreover, the higher magnification observation of these dendritic areas (bluish areas) which exhibit well defined striations (Figs. 6c, 6h) leads to an empirical estimation that where there was a blue area, there were striations.

For better understanding of the exact correlation between fatigue striation lines and dendritic structure, the striation lines located within primary dendritic cores are further characterised as shown in Fig. 7. A primary dendrite arm is indicated by red dashed box in Fig. 7a. This example was taken from the early crack propagation area which is very close to initiation site. Whereas, the primary dendrite arms can be easily observed at the end of the crack propagation area, see an example in Fig. 7c from H-C sample. As expected, the blue dendritic areas contained striation lines with a low crack propagation rate of ~ 360 nm / cycle in the very early crack propagation stage, see the shadowy striation lines in Fig. 7b which is the high magnified image of the red point in Fig. 7a. A high crack propagation rate of 0.9~1.3 μm / cycle is shown in Figs. 7d and 7e which are the high magnified areas in Fig. 7c.

Based on the results summarised above, a simplified model of striation line distribution within the dendritic structure is schematically presented in Fig. 7f. It shows the fatigue striation, which represents the trace of fatigue crack propagation process, is only limited in primary and secondary dendritic areas that are separated by interdendritic areas. Moreover, the crack propagation rate increases as the crack advances, signified with increasingly wider striation spacing along the propagation direction in the same figure. Furthermore, based on the elaborate measurement of striation spacings across the whole fracture surface for each sample, see further examples in Supplementary Fig. 4, the crack propagation rate versus crack length (i.e., the distance from initiation point) data is displayed in Fig. 7g. Here, the focus was on the grain size effects on the crack propagation rate rather than porosity, thus, the L-E data was not included in the graph as the crack started from a large pore cluster and the sample failed rapidly. For further clarification, the average of grain size for each sample are also listed in the same figure. It is evident that the crack propagation rate in the LCF samples are much higher than in the HCF samples after crack initiation stage. This is expected as much higher loading stress was applied during LCF test (~650 MPa) than in HCF (~335 MPa). Importantly, it is clear that the crack propagation rate in the large grain size sample is higher than in the small grain size samples during both LCF and HCF tests. As for HCF, a significant difference in facet size in each sample within the initiation zone was found, which might affect the starting point of striation development. Therefore, considering the slope of the crack propagation rate in HCF might be more indicative. It is showed that the slope in large grain (~1143 μm) sample H-T is higher than the small grain (~534 μm) sample H-E. Moreover, the greater crack propagation length in H-E is consistent with the result in Fig. 4h. A special notice should be given to H-C, for which the term 'crack propagation distance' should be used cautiously and will be further discussed in Section 4.3. However, with the largest grain size in H-C, it should be highlighted that the propagation stage with striation only covered a distance of ~200 μm and showed the largest slope of propagation rate.

3.2.2 Geometrically Necessary Dislocation (GND) distribution within dendritic structure

It is generally believed that geometrically necessary dislocation (GND) represent an extra storage of dislocations required to accommodate the lattice curvature resulted from non-uniform plastic deformation such as in two-phase system or polycrystalline material (Ashby, 1970). In contrast, the rest of dislocations which evolve from random trapping process and produce no long-range curvature in the lattice are termed as 'statistically stored dislocations (SSD)' (Ashby, 1970). It is also believed that GNDs act as obstacles to the motion of other SSDs and hence contribute to the work hardening of the material (Gao and Huang, 2003). The EBSD-based GND calculation employed here is based on misorientation data that can offer quantitative information on GND type dislocation distribution in micro-scale but cannot count for SSD type as they are not contributing to the lattice curvature. The GND mappings for large areas in L-T and H-E sample are shown in Fig. 8. The EBSD mappings were conducted just beneath the fracture surface of short crack propagation stage (blue areas), close to crack initiation site and parallel to the loading direction. Samples with highest fatigue life, largest crack propagation area under both LCF and HCF conditions, L-T (Fig. 8a-c) and H-E (Fig. 8d-f), respectively, are particularly chosen. The Nb EDS mapping was used to signify carbides distribution and dendritic structure, see Figs. 8b and 8e. The grain boundaries extracted from IPF maps in Figs. 8a and 8d are superimposed on the EDS maps and GND maps, see the white lines in Figs. 8b-c and 8e-f. The most striking feature in the GND maps is that the GND density distributions are nearly a reflection of dendritic structure in both examples. The high GND density (~3×10^2 μm^{-2}) was found to be in the interdendritic areas while the lowest density (~25 μm^{-2}) was found in the dendritic areas. In contrast, it seems that GND density have no apparent relationship with grain boundaries, especially in sample L-T, although the grains in the EBSD mapped area have different orientations. Furthermore, it appears that grain orientation effect on GND accumulation is negligible compared to the change caused by dendritic structure. This indicates that the critical role of dendritic structure can overcome the influence of orientation factor in this particular stress levels used in the current study. It is therefore, concluded here that GND density accumulation and distribution is more affected by the existing dendritic structure rather than grain boundary or crystallographic orientation. The GND relationship with striation distribution and hence on fatigue crack propagation will be discussed in detail in Sections 4.1 and 4.2.

3.2.3 STEM-based dislocation analyses

The dislocation density correlation with the dendritic structure is further studied via TEM-BF (bright field) and STEM-HAADF images. The area of interests (AOIs) were extracted using FIB technique as well as conventional thin TEM foil sample preparation. The exact FIB-extract sites are indicated on the SEM image and GND density map shown in Figs. 9a and 9b. The two extracted areas are carefully extracted from dendrite and interdendrite zones. The TEM-BF images of interdendritic and dendritic area are shown in Fig. 9c and Fig. 9d, respectively. Fig. 9c clearly shows high dislocation density within the interdendritic area along the γ channels. In contrast, almost free dislocation zone is found in dendritic area that featured an intact shape and orderly γ', see Fig. 9d. These TEM images also confirmed irregular morphology and slightly larger γ' in the interdendritic area compared with those in the dendritic area. Further dislocation distribution investigation was carried out using conventional thin foil specimens beneath crack propagation area of fracture surfaces.

Figs. 9e-f and 9g show dislocation density and morphology in typical interdendritic and dendritic area, respectively. Moreover, STEM-HAADF mode have been employed here as this technique provides high resolution and contrast for dislocation observation as reported in (Ding et al., 2018). Again, it shows much higher dislocation density in interdendritic area than dendritic area. It appears that the dislocations in interdendritic area are mostly accumulated around γ□ and especially between narrow γ channels, see Fig. 9e (BF) and Fig. 9f (HAADF). Fig. 9h-j directly compare the dislocation density in an adjacent interdendritic / dendritic area. According to the measurement method from Pesicka et al. (2003), it is evaluated that the average dislocation density in interdendritic area and dendritic area are ~250 and ~25 μm^{-2}, as shown in Fig. 9i and Fig. 9j, respectively. These dislocation density values are comparable to and in an agreement with the result from EBSD-based GND calculations. It should be remembered that the dislocations observed by TEM are consist of both GND-type and SSD-type dislocations. This indicates that most of the entangled dislocations observed in the interdendritic area in Fig. 9i are GND types. Recent reports on dislocation density (both GND and SSD) evolution by Zhu et al. (2018) and Muransky et al. (2019) suggest that in the early stage of plastic deformation when plasticity level is low (e.g., below 3% (Muransky et al. 2019) or 9% (Zhu et al. 2018)), the dominant dislocation type maybe GND-type. Whilst the results in the current study are in agreement with previous reports, one should be cautious when directly comparing the density of GNDs and SSDs. This is mainly because, (i) it is still difficult to distinguish GND from SSD via direct observation in TEM or STEM-HAADF image; (ii) the correct evaluation of total dislocation density is greatly affected by the measurement errors produced during TEM foil preparation (artificial dislocation) or the measurement of foil thickness of TEM specimen. This measurement error is also true for synchrotron diffraction peak analyses for dislocation density measurement (Muranksy et al. 2019). Moreover, EBSD-based measurement of GND density heavily depends on sample preparation, strain state, indexing rate, mapping step size and noise flour (Jiang et al. 2013). Therefore, the GND domination over SSD proposed here needs further validation.

3.3 Micro/Macro/Meso-texture and failure correlations

3.3.1 Facet formation and growth during HCF loading

Serial sectioning technique together with EBSD tool have been utilised to characterise the microstructure and crystallographic orientation distributions as well as their direct influence on crack initiation and propagation mechanisms. Parts of EBSD mapped sections that could reveal the key features have been presented in Figs. 10 and 11 for HCF samples, and in Fig. 12 for LCF samples. As stated in Section 3.1, the most predominant feature during HCF loading in nickel-based superalloy is the facet formation and growth in crack initiation stage. This is clearly demonstrated in the IPF//LD maps in Figs. 10 and 11. From the obtained EBSD data, the individual facet grain orientation with reference to the loading direction (LD) as well as the specific activated slip system and hence the Schmid Factor (SF) values of the individual slips can be resolved. The calculated slip traces and the highest SF values for each slip plane are also superimposed on the Figs. 10c, 10d and 11d. The results from overall serial sectioning data suggest that there is only one facet plane activated immediately after crack initiation (pore in this case) in sample H-T (Grain 1 (G1) in Fig. 10c) and sample H-C (G5 in Fig. 11d). While there are two facet planes in sample H-E (G3 and G4 in Fig. 10d) intersecting at the initiating pore site (Fig. 10b). It is not surprising to see in a sample with relatively small grain and pore size, such as in H-E, both facet planes were activated along a slip system with highest SF values, i.e., 0.43 of (1-11) slip plane in G3 and 0.44 of (-111) slip plane in G4, which have been highlighted in red colour and the red slip traces in Fig. 10d. However, in the samples with large grain and pore sizes, such as in H-T and H-C, the activated slip plane has the third highest SF values, 0.39 of (-111) in G1 and even as small as 0.28 of (-111) in G5, as highlighted in yellow colour in Figs. 10c and 11d, respectively. It should be noted here that Schmid factor calculation is based on the validity of the external uniaxial stress state within individual grains without considering additional local stresses. However, it has been reported that the effective SFs might be affected by local stress states generated by precipitates, adjacent grains or residual stress (Peralta and Laird, 1998). Here, it is assumed that the pore with large size and non-homogenously distributed may influence the stress state locally. Indeed, the high GND density near large pore sizes as previously shown in Supplementary Fig. 3c can act as a stress raiser for crack initiation, which effectively validate the local stress state role on deformation mechanisms. Therefore, it is concluded that when the pore size is large enough to induce large local stress changes, the effective slip system that actually activated does not necessarily have the highest nominal SF value.

Fig. 11b shows the EBSD maps of two parallel cross section for both halves of the failed bars. This quasi 3-D view was needed to validate that the facet size is limited by faceted grain size. As shown in Fig. 11b. the facet length is determined by the grain size. In CS 2, the facet plane is constrained in between G9 and G10. Whereas in CS 3 the same facet length is constrained by G8 and G10 (Fig. 11b). A similar observation was found in other two HCF samples. For example, in CS 2 of H-T sample (Fig. 10a), the facet plane in G1 is restricted by the underlaying grain that has a <101>//LD orientation, and in CS 3 of H-E, the facet plane in G4 is restricted by G3 (Fig. 10d).

3.3.2 Crack propagation in relation with crystallographic structure during LCF loading

The cross sections (CS)s of three LCF samples are shown in Fig. 12. The quasi 3-D mapping implemented here could successfully identify the crack initiation sites (pores). For instance, the pores cluster in the sample L-E is observed to be at the triple junction of three grains, i.e., G3 (Grain 3), G4 and G5, as indicated in CS 4 of Fig. 12b. It is also observed that grain boundaries can affect the crack tip location where the crack transits from crack propagation (Stage II) to overload stage (Stage III). An example is shown in Fig. 12c, two intersection sites between CS 2, CS 4 and crack transition line (indicated as white line) are identified at grain boundary points (red arrows on the fracture surface), as also indicated by two red arrows in IPFs of these two CSs. Further two examples on this phenomenon in HCF samples are displayed in Supplementary Fig. 5, showing the barrier effect of grain boundary on the final stage of crack propagation. Moreover, it is important to be pointed out that both in LCF and HCF samples, combining fracture surface and beneath IPFs, crack propagation stage in small grain size samples, such as L-T (Fig. 12a) and H-E (Fig. 10b), covered 4~5 grains, whilst large grain samples such as L-C (Fig. 12c) and H-T (Fig. 10a) covered only 1~2 grains. It is finally established that the number of the grains and grain boundary distribution within the tested sample have a significant influence on crack propagation as well as overload boundary location. This has affected the overall fatigue property of the tested bars that contained different numbers of grains.

4. Discussion

4.1 On the role of dendritic structure during crack propagation stage

The results showed that fatigue striations, the unique traces of crack propagation process, are only limited in dendritic core areas. In other words, intermittent striation areas are separated by interdendritic areas (Fig. 6 and Fig. 7). It appears that the dendritic core area provided a path unit for crack propagation. Fig. 7f has schematically showed the striation distribution within the dendritic structure along the crack propagation path. The complete set of microscopic and macroscopic data in the current study were collected to describe the exact crack propagation mechanism in IN713C alloy and it is summarised in Fig. 13. The striation structure during different stages of crack growth are schematically shown in Fig. 13. The grain size effect on crack path is also considered, however, little differences in dendrite/crack propagation correlation was found either in an individual large grain or in a small multi-grain cluster, see Figs. 13a-c and 13d-f, respectively. It should be emphasised here that no significant difference in the effect of loading mode, LCF and HCF, on the striation distribution and its relationship with dendritic structure has been observed during crack propagation stage. Thus, the following discussion is based on the general observation in the fatigue tests of IN713C.

It is anticipated to have a minimum GND density prior to the fatigue loading in the original untested IN713C alloy in both large grain and small grain cluster, see Figs. 13a and 13d, respectively. As demonstrated in Figs. 13b and 13e, after the initial stage of loading, a crack is initiated from a casting defect. During the early stage of crack growth, the GNDs are accumulated within interdendritic areas, which has been demonstrated by both EBSD-based GND calculations (the highlight in Fig. 13c, f, and Fig. 8) and TEM observations (the highlight in Fig. 13b and Fig. 9).

The high GNDs density in interdendritic areas are largely generated around carbides as reported in our previous investigation (Liu et al., 2018) and partly around irregular shape γ'. This is because most of carbides are segregated in interdendritic area and there are contrasting deformation ability between carbides and γ matrix, resulting in tremendous strain gradient and GNDs around carbides when imposed to cyclic loading (Liu et al., 2018; Karamched and Wilkinson, 2011).Moreover, the high lattice misfit between γ' and γ in interdendritic area (compared to those in dendritic area) that is represented by the irregular γ' morphology leads to high stress field which effectively resist further dislocation motion via dislocation entanglement mechanism, causing strain hardening. Thus, the high GNDs density together with lower dislocation mobility that contribute to the interdendritic area strengthening, create a microstructure unit of "hard" interdendritic area surrounding much "softer" dendritic area. This explains the crack preferential propagation through the "soft" dendritic area, leaving visible fatigue striation in this area, as schematically shown in Figs. 13b and 13e.

Here, we propose a concept of 'crack propagation unit (CPU)' based on the regular distribution of striation and dislocation in relation to the dendritic structure. This CPU consists of one secondary dendritic area and one adjacent interdendritic area, and the average diameter of this unit essentially equals to the secondary dendrite arm spacing, d, as shown in Fig. 13g. In this unit structure, we emphasise the role of secondary dendritic area is due to, first, we believe most of volume fraction of the material consist of secondary dendritic/interdendritic structure as tertiary dendritic structure has hardly been observed in the samples; second, primary dendritic area itself alone is a 'soft' area and assumed to have little contribution in strengthening and crack advance resistance. Therefore, this

CPU represents the basic unit of crack propagation in relation to the microstructure (dendrite/interdendrite) and best reflect the dislocation density distribution patterns. As cyclic loading continues, the crack advances following ‘interdendritic area hardening and dendrite facilitating easy crack propagation’ mechanisms. With increase in crack length, the crack propagation rate increases, which is represented by wider striation spacing, as shown in Figs. 13c and 13f.

The relationship between fatigue striation distribution (morphology) and dendritic structure proposed here is in agreement with our study on real turbine blade component (Liu et al., 2018). From Liu et al. (2018) it was clear that the large area of fine long striations was observed during HCF failed location where weak dendritic structure present. Whereas, only local and separated striation lines during crack propagation stage was observed in LCF failed location where obvious dendritic structure exhibited (Liu et al., 2018).

4.2 On the role of grain size during crack propagation stage

The results from fatigue tests in this study show beneficial effect of smaller grain size on fatigue life during both LCF and HCF loadings (Figs. 4d and 4h). Moreover, a slower crack propagation rate in smaller grain size samples has also been observed (Fig. 7g). The Hall-Petch relation is usually used to describe the improved strength with decreasing grain size. As the grain boundary is believed not only impeding the dislocation movement leading to dislocation pile up, but also acts as source of dislocation nucleation (Kacher et al., 2014). It should be mentioned that the original form of Hall-Petch is valid for single-phase materials and monotonic loading only. However, this relation has been modified and extended to multi-phase materials subjected to cyclic loading conditions as long as planar slip prevails. For instance, it is modified by combining the contribution of the different types of boundaries (e.g., phase boundary and grain boundary) to the yield stress (Fan et al., 1993) and by replacing the monotonic yield stress with the cyclic yield stress. Moreover, the modified Hall-Petch relation has found success in modelling and predicting fatigue crack propagations (Düber et al., 2006).

It has been reported that fatigue crack propagation rate increases with increasing grain size (Shao et al., 2017; Krupp, 2007). This is due to the effective slip length that depends on the alloy grain size and geometry. In coarse grain size materials, the effective slip length can be as large as the grain size and accommodate large numbers of dislocations. This in effect generate significant strain incompatibility with the adjacent grains, and hence promoting slip and later crack transfers across the grain boundaries. The hypothesis above anticipated large numbers of dislocations along grain boundaries, which, however, is not the case in the present study. Instead, a large amount of dislocations (GNDs) distributed in interdendritic areas rather than grain boundaries, as described in Section 4.1 and schematically illustrated in Fig. 13. This is partly due to the difference between single phase materials where the above theorises mainly applied and γ' precipitated hardened IN713C alloy, where the dislocation mainly generate and accumulate in the γ channel before moving toward interdendritic area and grain boundaries. However, it appears that the stress level used during both LCF and HCF loading was not high enough to push a mass of dislocation from the interdendritic area toward the grain boundaries.

As described in Section 4.1, the concept of CPU was proposed as individual clusters of secondary dendritic area and interdendritic area, rather than individual grains. Therefore, it is reasonable to modify the Hall-Petch relation by replacing the mean grain size with mean CPU size (secondary dendrite arm spacing) in this dendritic structure containing alloy. However, the CPU size or secondary dendrite arm spacing is in the same order in all the samples investigated, regardless of different grain size. Therefore, a plausible explanation for the higher resistance to fatigue propagation in smaller grain size sample is the complex configuration of dendritic structure across different grains, as schematically explained in Fig. 13.

For comparison purposes, the same surface crack propagation area, i.e., same crack front length, in only one single large grain in Figs. 13a-c (representing crack in large grain size sample) and three small grains in Figs. 13d-f (representing crack in multi-grains sample) is shown. In the latter case, the small grains have different orientations and form different dendritic structure during solidification process, as shown in Fig. 13d. At the early crack growth stage, the crack grows along CPUs and there is no significant difference in propagation rate between large grain and small clustered grains, as shown in Figs. 13b and 13e, respectively. However, in the later stage, the crack growth continues without changing directions in large single grain, see Fig. 13c, and decelerate in multiple grains case, see Fig. 13f. This deceleration in the latter case is attributed to the dendrite direction changes in the adjacent grains. As the crack fronts within individual dendritic area have to adjust to accommodate the abrupt change of direction and maintain continuity. Frequent such accommodation hence hinder the crack propagation, as shown in Fig. 13f and Fig. 13h. It should be noted here, this is a simplified model with a small grain numbers and demonstrated only in 2-D, thus, the effect of grain size in 3-D will be even greater. For instance, in only one-dimension (1-D) situation, it showed that crack propagation area in smaller grain size sample covered ~5 grains (L-T, see Fig. 12a), in contrast with ~2 grains in large grain size sample (L-C, see Fig. 12c). However, this difference in grain numbers becomes 25 (5×5) versus 4 (2×2) after realising that the crack propagation is at least a 2-D event.

This model proposed here signify the beneficial effect of smaller grain size on fatigue crack propagation resistance. More importantly, the adaptation of crack propagation unit (CPU) into Hall-Petch relation can lead to better understanding of the effect of heterogeneous structure on fatigue crack propagation. This aspect needs to be further verified by carefully controlled experiment and modelling. However, based on this preliminary experiment results, it would be useful to take into account the concept of crack propagation unit when modelling fatigue crack propagation in cast alloys. This has been partly achieved by the simulation work of Lee et al. (Gao et al., 2004; Yi et al., 2006) where they proposed a very similar concept, i.e., micro-cell, to determine fatigue crack initiation and crack propagation in casting Al alloy. The core elements in the micro-cell were the dendritic structure and Si particles. One of the key parameters in their model was secondary dendrite arm spacing (λ_2), which agrees well with our key parameter proposed here. While they obtained agreed predicted fatigue life with experimental measured life using finite element (FE) modelling, little correlation of the crack propagation path with the microstructure features and substructure features such as dislocation density distribution was demonstrated. Whereas detailed experimental microstructure observation is reported in the present work. This kind of micro-mechanism research based on detailed microstructure characterisation and analyses are believed to be critical to validate these cell/unit models.

4.3 On the role of crystal orientation during crack propagation stage

According to Neumann model (1969), fatigue crack propagation process is dominated by alternate activation of slip systems and leads to the formation of striations on the fracture surface. In nickel-based superalloy (FCC structure) these slip systems are {111} slip systems, and the propagation process is essentially orientation dependant. The example shown in Fig. 14 clearly demonstrates the effect of grain orientation on fatigue crack path. The fracture surface study for H-C sample in Fig.14a (same sample in Figs. 4g, 7c and 11a) shows that there is a unique large flat area immediately after initiation pore site crossing two grains (G7 and G8 in Fig. 11d) on which dendritic structure is apparently visible as indicated in Fig. 14a. Between this area and overloading area there is a narrow 'propagation area' identified via striations lines analyses. This propagation area indicated in Fig. 14a is further magnified in Fig. 14b showing 3 points of interest. This narrow area is only 200 μm in width as indicated by two red dashed lines in Fig. 14a, see also the colour contrast in Fig. 14b. Within the area, it is observed that only few faded striation lines were found at the interfacing area (Area 1 as indicated in Fig. 14b) and very fine striation lines as propagation 'starts' with small striation spacings (0.4 μm / cycle) in Area 2, quickly followed by large propagation rate (0.8 μm / cycle) in Area 3. The large flat area that featured a visible dendritic structure is termed here as 'brittle cracking area' due to its rapid cracking (brittle) without alternate slip systems activating process. This phenomenon is believed to be related to the grain orientation with respect to the loading direction. In the model proposed by Bowles and Broek (1972), it is assumed that the crack propagation occurs by a slip decohesion mechanism with at least two acting planes. The crack plane is the plane bisecting the two operating {111} slip planes and can be either along (001) (Fig. 14e) or (110) (Fig. 14f) planes. In the case of (001) crack plane, for instance, two slip planes, as schematically shown in Fig. 14e, (1-11) in the upper unit and (-111) in the lower cell will result in the new (001) crack plane if taking effective Burgers vector into account (Duber et al., 2006). Therefore, when the (001) plane is perpendicular to the loading direction (<001>// LD), i.e., Cube orientation, the (111) family slip should be on 45 degrees angle with the loading direction to facilitates a pure shear condition, thus Cube is generally believed to be soft and easy to activate octahedral (111) slip system. However, the shear condition in both (1-11) and (-111) slip planes will allow a crack propagation perpendicular to the LD which is <001> in this case.

It has also been reported that the preferable and fast-growing direction for dendrite growth during solidification for nickel-based superalloy is <001> direction (Zhou et al., 2008). This is confirmed by the dendritic structure and morphology shown in Figs. 14c and 14d. This dendrite growth direction parallel to crack direction (perpendicular to loading direction) might also contribute to the significant large crack propagation rate in this brittle cracking area. Overall, it is concluded that grains with Cube orientation (<001>//LD) will tremendously facilitate crack propagation by offering readily propagation planes along dendrite growth direction.

5. Conclusions

IN713C nickel-based superalloy produced via investment casting were tested under LCF and HCF conditions at 650°C. An exhaustive characterisation and analysis were conducted on fractured samples surface in 2-D and quasi 3-D via the utilisation of SEM, TEM, STEM-HADDF and HR-EBSD. Here, the fatigue crack propagation micromechanism in cast alloy is proposed and directly correlated to the dendritic structure, grain size and crystallographic orientation produced during solification. The major conclusions from this study are:

1. Fatigue striations were only observed in dendritic areas, separated by interdendrite channels.

2. EBSD-based GND mapping and STEM-HAADF dislocation imaging showed a unique dendritic structure dependent dislocation distribution patterns that dislocation density in interdendirtic area is much higher than in dendritic area.
3. The individual secondary dendrite volume and its adjacent inderdendritic area are considered to be a critical parameter in fatigue crack propagation and acted as crack propagation unit (CPU), considering the striation and dislocation density distribution.
4. Large grain size microstructure shows higher crack propagation rate than small grain microstructure. This beneficial effect of small grain size is believed to be due to the frequent change of propagation directions of the CPU rather than to be controlled by dislocation accumulation at the grain boundary.
5. Under HCF condition, in the case of large pore size and hence large local stress around pore, it is not necessary for the facet to occur on the highest SF plane. Having large volume fraction of <100> // LD, i.e., Cube orientation within crack propagation area will facilitate crack propagation as <100> direction is the bisection plane of two {111} slip planes and is the preferable direction for dendrite growth.
6. Small grain size IN713C nickel-based superalloy is recommended for both LCF and HCF properties. Higher LCF life in fine grain microstructure is largely due to the deceleration of the crack propagation rate. Whereas, during HCF test, the small grain sizes assisted in slower crack growth rate and generated small facet size which greatly assisted in crack growth constraining.

Acknowledgements

The authors would like to thank CSC (Chinese Scholarship Council) and College of Engineering in Swansea University for the project funding and facilities support in AIM (Advanced Imaging of Materials) in Swansea University. This paper is dedicated to the celebration of 100 anniversary of

Lanzhou University of Technology, in which G. Liu spent an unforgettable four years for his undergraduate.

References

Ashby, M., 1970. The deformation of plastically non-homogeneous materials, Philos. Mag. 21(170), 399-424.

Birosca, S., Di Gioacchino, F., Stekovic, S., Hardy, M., 2014. A quantitative approach to study the effect of local texture and heterogeneous plastic strain on the deformation micromechanism in RR1000 nickel-based superalloy. Acta Mater. 74, 110-124.

Birosca, S., Liu, G., Ding, R., Jiang, J., Simm, T., Deen, C., Whittaker, M., 2019. The dislocation behaviour and GND development in a nickel-based superalloy during creep. Int. J. Plast 118, 252-268.

Bowles, C., Broek, D., 1972. On the formation of fatigue striations. Int. J. Fract.Mech. 8, 75-85.

Cai, H., McEvily, A., 2001. On striations and fatigue crack growth in 1018 steel. Mater. Sci. Eng. A 314, 86-89.

Chan, K.S., 2010. Roles of microstructure in fatigue crack initiation. Int. J. Fatigue 32, 1428-1447.

Chen, B., Jiang, J., Dunne, F.P.E., 2018. Is stored energy density the primary meso-scale mechanistic driver for fatigue crack nucleation? Int. J. Plast 101, 213-229.

Coleman, M., Alshehri, H., Banik, R., Harrison, W., Birosca, S., 2016. Deformation mechanisms of IN713C nickel-based superalloy during Small Punch Testing. Mater. Sci. Eng. A 650, 422-431.

Dezecot, S., Maurel, V., Buffiere, J.-Y., Szmytka, F., Koster, A., 2017. 3D characterization and modeling of low cycle fatigue damage mechanisms at high temperature in a cast aluminum alloy. Acta Mater. 123, 24-34.

Ding, Q., Li, S., Chen, L.-Q., Han, X., Zhang, Z., Yu, Q., Li, J., 2018. Re segregation at interfacial dislocation network in a nickel-based superalloy. Acta Mater. 154, 137-146.

Ding, R., Gong, J., Wilkinson, A.J., Jones, I.P., 2016. A study of dislocation transmission through a grain boundary in hcp Ti–6Al using micro-cantilevers. Acta Mater. 103, 416-423.

Düber, O., Künkler, B., Krupp, U., Christ, H.J., Fritzen, C.P., 2006. Experimental characterization and two-dimensional simulation of short-crack propagation in an austenitic–ferritic duplex steel. Int. J. Fatigue 28, 983-992.

Dunne, F.P.E., Wilkinson, A.J., Allen, R., 2007. Experimental and computational studies of low cycle fatigue crack nucleation in a polycrystal. Int. J. Plast 23, 273-295.

Dunstan, D.J., Bushby, A.J., 2014. Grain size dependence of the strength of metals: The Hall–Petch effect does not scale as the inverse square root of grain size. Int. J. Plast 53, 56-65.

Fan, Z., Tsakiropoulos, P., Smith, P.A., Miodownik, A.P., 1993. Extension of the Hall-Petch relation to two-ductile-phase alloys. Philos. Mag. A 67, 515-531.

Gao, H., Huang, Y., 2003. Geometrically necessary dislocation and size-dependent plasticity. Scr. Mater. 48, 113-118.

Gao, Y.X., Yi, J.Z., Lee, P.D., Lindley, T.C., 2004. A micro-cell model of the effect of microstructure and defects on fatigue resistance in cast aluminum alloys. Acta Mater. 52, 5435-5449.

Gelmedin, D., Lang, K.-H., 2010. Fatigue behaviour of the superalloy IN 713C under LCF-, HCF- and superimposed LCF/HCF-loading. Procedia Engineering 2, 1343-1352.

Grilli, N., Janssens, K.G.F., Nellessen, J., Sandlöbes, S., Raabe, D., 2018. Multiple slip dislocation patterning in a dislocation-based crystal plasticity finite element method. Int. J. Plast 100, 104-121.

Herbig, M., King, A., Reischig, P., Proudhon, H., Lauridsen, E.M., Marrow, J., Buffière, J.-Y., Ludwig, W., 2011. 3-D growth of a short fatigue crack within a polycrystalline microstructure studied using combined diffraction and phase-contrast X-ray tomography. Acta Mater. 59, 590-601

Horstemeyer, M.F., Yang, N., Gall, K., McDowell, D.L., Fan, J., Gullett, P.M., 2004. High cycle fatigue of a die cast AZ91E-T4 magnesium alloy. Acta Mater. 52, 1327-1336.

Huang, E.W., Barabash, R.I., Clausen, B., Liu, Y.-L., Kai, J.-J., Ice, G.E., Woods, K.P., Liaw, P.K., 2010. Fatigue-induced reversible/irreversible structural-transformations in a Ni-based superalloy. Int. J. Plast 26, 1124-1137.

Jiang, J., Britton, T.B., Wilkinson, A.J., 2013. Measurement of geometrically necessary dislocation density with high resolution electron backscatter diffraction: Effects of detector binning and step size. Ultramicroscopy 125, 1-9.

Jiang, J., Yang, J., Zhang, T., Zou, J., Wang, Y., Dunne, F.P.E., Britton, T.B., 2016. Microstructurally sensitive crack nucleation around inclusions in powder metallurgy nickel-based superalloys. Acta Mater. 117, 333-344.

Kacher, J., Eftink, B.P., Cui, B., Robertson, I.M., 2014. Dislocation interactions with grain boundaries. Curr. Opin. Solid State Mater. Sci. 18, 227-243.

Karamched, P.S., Wilkinson, A.J., 2011. High resolution electron back-scatter diffraction analysis of thermally and mechanically induced strains near carbide inclusions in a superalloy. Acta Mater. 59, 263-272.

Kontis, P., Alabort, E., Barba, D., Collins, D.M., Wilkinson, A.J., Reed, R.C., 2017. On the role of boron on improving ductility in a new polycrystalline superalloy. Acta Mater. 124, 489-500.

Krupp, U., 2007. Fatigue crack propagation in metals and alloys: microstructural aspects and modelling concepts. John Wiley & Sons.

Kunz, L., Lukáš, P., Konečná, R., 2010. High-cycle fatigue of Ni-base superalloy Inconel 713LC. Int. J. Fatigue 32, 908-913.

Larrouy, B., Villechaise, P., Cormier, J., Berteaux, O., 2015. Grain boundary–slip bands interactions: Impact on the fatigue crack initiation in a polycrystalline forged Ni-based superalloy. Acta Mater. 99, 325-336.

Liu, G., Salvat Cantó, J., Winwood, S., Rhodes, K., Birosca, S., 2018. The effects of microstructure and microtexture generated during solidification on deformation micromechanism in IN713C nickel-based superalloy. Acta Mater. 148, 391-406.

Miao, J., Pollock, T.M., Jones, J.W., 2009. Crystallographic fatigue crack initiation in nickel-based superalloy René 88DT at elevated temperature. Acta Mater. 57, 5964-5974.

Muránsky, O., Balogh, L., Tran, M., Hamelin, C.J., Park, J.S., Daymond, M.R., 2019. On the measurement of dislocations and dislocation substructures using EBSD and HRSD techniques. Acta Mater. 175, 297-313.

Neumann, P., 1969. Coarse slip model of fatigue. Acta Metall. 17, 1219-1225.

Peralta, P., Laird, C., 1998. Fatigue fracture at bicrystal interfaces: experiment and theory. Acta Mater. 46, 2001-2020.

Pešička, J., Kužel, R., Dronhofer, A., Eggeler, G., 2003. The evolution of dislocation density during heat treatment and creep of tempered martensite ferritic steels. Acta Mater. 51, 4847-4862.

Petrenec, M., Obrtlík, K., Polák, J., 2005. Inhomogeneous dislocation structure in fatigued INCONEL 713 LC superalloy at room and elevated temperatures. Mater. Sci. Eng. A 400-401, 485-488.

Pineau, A., McDowell, D.L., Busso, E.P., Antolovich, S.D., 2016. Failure of metals II: Fatigue. Acta Mater. 107, 484-507

Pirgazi, H., Ghodrat, S., Kestens, L.A.I., 2014. Three-dimensional EBSD characterization of thermo-mechanical fatigue crack morphology in compacted graphite iron. Mater. Charact. 90, 13-20.

Pollock, T.M., Tin, S., 2006. Nickel-based superalloys for advanced turbine engines: chemistry, microstructure and properties. J. Propul. Power 22, 361-374.

Reed, R.C., 2008. The superalloys: fundamentals and applications. Cambridge university press.

Riemelmoser, F., Pippan, R., Stüwe, H., 1998. An argument for a cycle-by-cycle propagation of fatigue cracks atsmall stress intensity ranges. Acta Mater. 46, 1793-1799.

Salvat Cantó, J., Winwood, S., Rhodes, K., Birosca, S., 2018. A study of low cycle fatigue life and its correlation with microstructural parameters in IN713C nickel-based superalloy. Mater. Sci. Eng. A 718, 19-32.

Shao, C.W., Zhang, P., Zhu, Y.K., Zhang, Z.J., Pang, J.C., Zhang, Z.F., 2017. Improvement of low-cycle fatigue resistance in TWIP steel by regulating the grain size and distribution. Acta Mater. 134, 128-142.

Stinville, J.C., Martin, E., Karadge, M., Ismonov, S., Soare, M., Hanlon, T., Sundaram, S., Echlin, M.P., Callahan, P.G., Lenthe, W.C., Miller, V.M., Miao, J., Wessman, A.E., Finlay, R., Loghin, A., Marte, J., Pollock, T.M., 2018. Fatigue deformation in a polycrystalline nickel base superalloy at intermediate and high temperature: Competing failure modes. Acta Mater. 152, 16-33.

Thompson, A.W., Backofen, W.A., 1971. The effect of grain size on fatigue. Acta Metall. 19, 597-606.

Yi, J.Z., Gao, Y.X., Lee, P.D., Lindley, T.C., 2006. Microstructure-based fatigue life prediction for cast A356-T6 aluminum-silicon alloys. Metallurgical and Materials Transactions B 37, 301-311.

Zaefferer, S., Wright, S.I., Raabe, D., 2008. Three-Dimensional Orientation Microscopy in a Focused Ion Beam–Scanning Electron Microscope: A New Dimension of Microstructure Characterization. Metallurgical and Materials Transactions A 39, 374-389.

Zhai, T., Wilkinson, A.J., Martin, J.W., 2000. A crystallographic mechanism for fatigue crack propagation through grain boundaries. Acta Mater. 48, 4917-4927.

Zheng, Z., Balint, D.S., Dunne, F.P.E., 2017. Investigation of slip transfer across HCP grain boundaries with application to cold dwell facet fatigue. Acta Mater. 127, 43-53.

Zhou, Y.Z., Volek, A., Green, N.R., 2008. Mechanism of competitive grain growth in directional solidification of a nickel-base superalloy. Acta Mater. 56, 2631-2637.

Zhu, C., Harrington, T., Gray, G.T., Vecchio, K.S., 2018. Dislocation-type evolution in quasi-statically compressed polycrystalline nickel. Acta Mater. 155, 104-116.

Table Captions:

Table 1 IN731C chemical composition (wt.%).

Figure Captions:

Fig. 1 Received bars with three different grain structures: T(Transition), E(Equiaxed) and C(Columnar). (a) and (b) Real size material and schematic bars, respectively; (c-e) IPFs (Inverse Pole Figures) // solidification direction (also loading direction (LD)) of these bars show grain structures. Scanned areas are shown in (b) and notice that they are cut and separately scanned due to very large area; (f) Average grain size of these structures.

Fig. 2 Representative microstructure in received materials: (a) Dendritic structure within three grains, dashed lines show grain boundaries; (b) Carbides segregating in interdendritic area; (c) and (d) γ' in dendritic area and interdendritic area, respectively; Magnified area in (c) shows very small γ' in γ channels.

Fig. 3 Grain structure around actual fractured area in tested bars: IPFs in (c-e) for LCF and (f-h) for HCF; (a) A representative failed bar (L-C) with major dimension size; (b) Schematic half fractured sample with sectioning planes showing EBSD scan position (only two cross sections (CS) shown here). To examine assumed transition structure, both half fractured samples are characterised and displayed. The results show no transition structure in the centre of the bar with 'nominal' transition structure.

Fig. 4 Fracture surface and fatigue life in LCF (a-d) and HCF (f-i) samples. (a-c) Fracture surface for L-T (LCF-Transition), L-E and L-C, respectively. (e-g)) Fracture surface for H-T (HCF-Transition), H-E and H-C, respectively. (d) and (h) Fatigue life (cycles) and crack propagation distance measured by the yellow double arrows for LCF and HCF, respectively. Red arrows in (a-c) indicate crack initiation sites, white dashed lines distinguish crack propagation stages and red dashed lines indicate EBSD position in Fig. 3.

Fig. 5 General features in sequential crack propagation stages, exemplified from sample L-T. (a) Illustration of propagation stages with striations (black curved lines) superimposed. (b) and (c) Part of whole fracture surface by OP and SEM, respectively. (d-g) Fatigue striations as major characteristics are shown in each stage corresponding to the area in (c). (h-k) γ' morphology immediately beneath the fracture surface in (d-g) individually. Very thin oxidation layer can be noticed, and the thickness are indicated by double dotted lines in (h) and (j).

Fig. 6 Secondary dendritic structure and striation distribution. (a-d) from sample L-C, (e-h) from sample H-E and (i) from sample L-E. (a, b) and (e-g) show the dendritic structure on fracture surface; (c) and (h) show the striations in dendritic area; (d) Dendritic structure in the sample and the average size of secondary dendrite is comparable to dendrite size on fracture surface in (b). The color contrast in (a), (e) and (i) reflect the dendritic structure, as indicated in (i).

Fig. 7 Primary dendritic structure and striation distribution. (a, b) from L-T, (c-e) from H-C. Primary dendrite are shown in red dashed circles in (a) and representative fine striations close to initiation site is shown in (b). Primary dendrites are shown by color contrast in (c) and striations are magnified in (d, e). (f) Schematically illustration of dendritic structure (both primary and secondary) and striation distribution. (g) Grain size dependence of crack growth rate, obtained from measurement of width of striations, as displayed in (b, d, e) and in other figures for example.

Fig. 8 Dendritic structure dependent GND density distribution based on EBSD data. (a-c) from sample L-T and (d-f) from sample H-E. (a, d) IPFs//LD show grain orientation and grain structure; (b, e) Element mapping of Nb showing dendritic structure in the same area in (a, d), respectively; (c, f) GND density mapping with grain boundaries superimposed by white lines. Step size of 200 nm was used.

Fig. 9 Dendritic structure dependent dislocation distribution based on TEM and STEM-HADDF. (a-d) Specimen from FIB (Focused Ion Beam) extracted site; (e-j) Specimen from electric polishing. (c, d) BF (Bright Field) images of dislocation in interdendritic area and dendritic area, respectively; (e, f) BF and STEM-HADDF images showing dislocation around γ' in a typical interdendritic area, respectively; (g) HADDF image in a typical dendritic area. (h-j) HADDF images in an adjacent interdendritic/dendritic area showing much higher dislocation density in interdednrite. Some dislocations are indicated by red arrows in (e, f).

Fig. 10 Grain orientation and structure distribution across the fracture surface revealed by serial sectioning method in sample H-T (a, c) and H-E (b, d), parts of IPFs // LD are displayed corresponding to the red dashed sectioning lines in (a, b). Calculated slip traces for {111} slip planes in facet grain(s) are superimposed and the highest Schmid factor value for each slip plane are displayed for each facet grain in (c, d).

Fig. 11 Grain orientation and structure distribution across the fracture surface in sample H-C. Parts of IPFs // LD (c) are displayed corresponding to the red dashed sectioning lines in (a). Calculated slip traces for {111} slip planes in facet grains (G5, G6 and G7) are superimposed and the highest Schmid factor value for each slip plane are displayed for each facet grain in (d). (b) Both top and bottom half of fractured sample at some locations are sectioned and EBSD scanned to reveal the whole facet grain. (e) Intersection of three grains that produce the pore.

Fig. 12 Grain orientation and structure distribution across the fracture surface in sample L-T (a), L-E (b) and L-C (c). Parts of IPFs // LD are displayed corresponding to the red dashed sectioning lines. The red arrows in (c) indicate the grain boundary.

Fig. 13 Schematic showing the grain size dependence of crack propagation rate and the dendritic structure dependence of dislocation distribution. (a-c) for large single grain; (d-f) for small multi-grains. The real dendritic structures are shown in the highlight of (a, d) and the real striation within dendritic area is shown in the highlight of (e). Dislocation segregated in interdendritic areas are proved both by GND mapping (the highlight in (c, f)) and HAADF images (the highlight in (b)). (g) Schematic illustration of crack propagation unit (CPU), and the diameter of CPU, ‘d’. (h) Schematic illustration of crack propagation rate versus crack length in different grain size samples.

Fig.14 Orientation dependent crack propagation rate, an example from sample H-C. (a) Between initiation pore and real ‘propagation’ area there is a large flat area where dendritic structure is visible. (b) The mirror surface of (a) in another half sample, and striations in different position of the narrow propagation area are magnified in 1-3. (c, d) cross section showing the dendritic structure by OP and crystallographic orientation, respectively. The sectioning line is shown with white dashed line in (a). (e, f) Schematically shows the mechanism of macroscopic fatigue crack propagation directions.

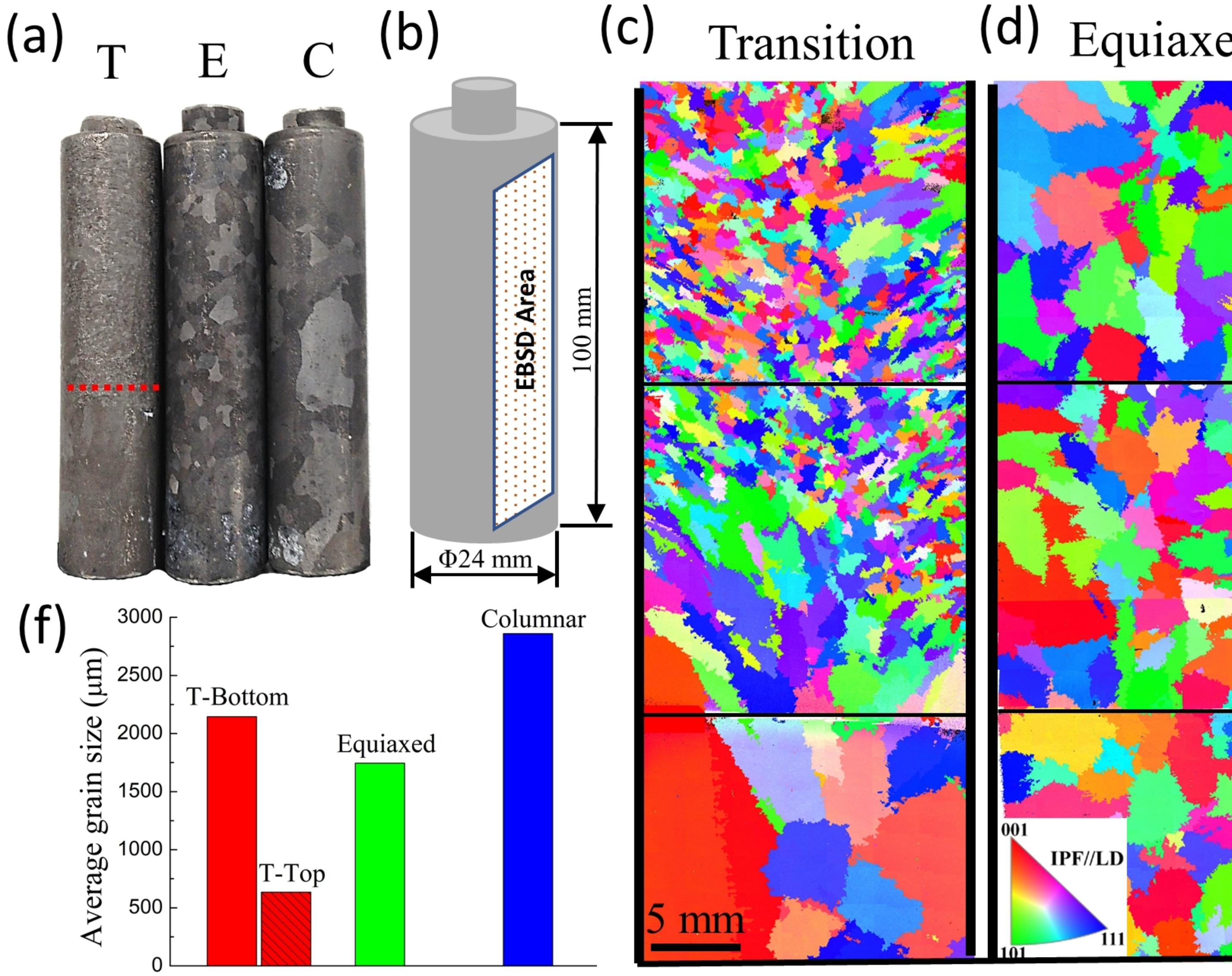
(a)
T
E
C
(b)
EBSD Area
100 mm
Φ24 mm
(c)
Transition
(d)
Equiaxe
5 mm
001
IPF//LD
111
101
(f)
Average grain size (μm)
3000
2500
2000
1500
1000
500
0
T-Bottom
T-Top
Equiaxed
Columnar

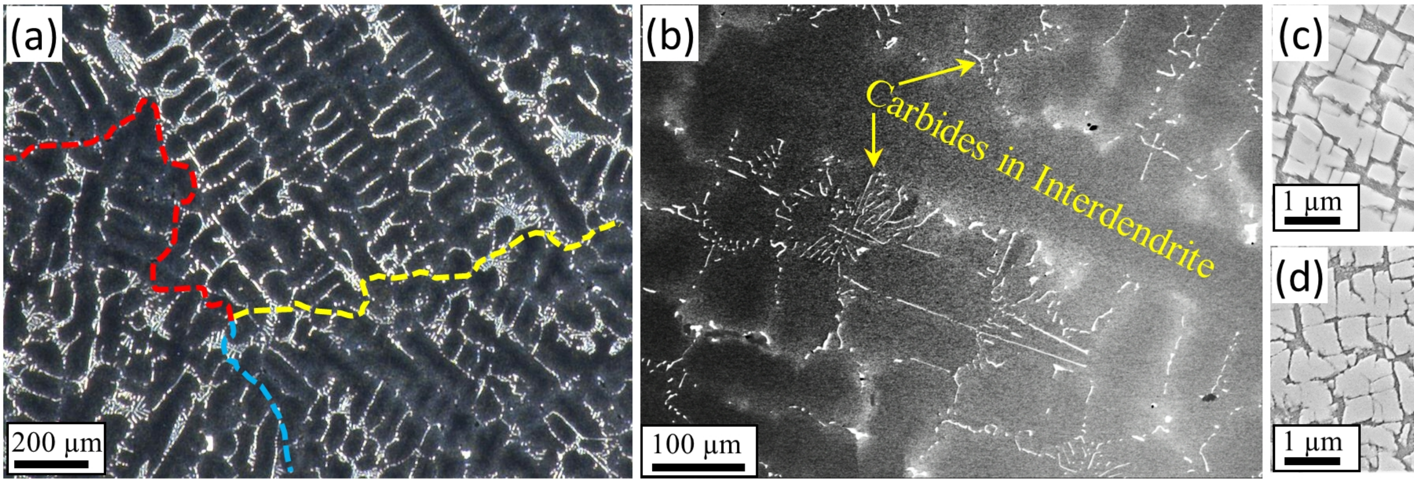
(a)
200 μm
(b)
Carbides in Interdendrite
100 μm
(c)
1 μm
(d)
1 μm

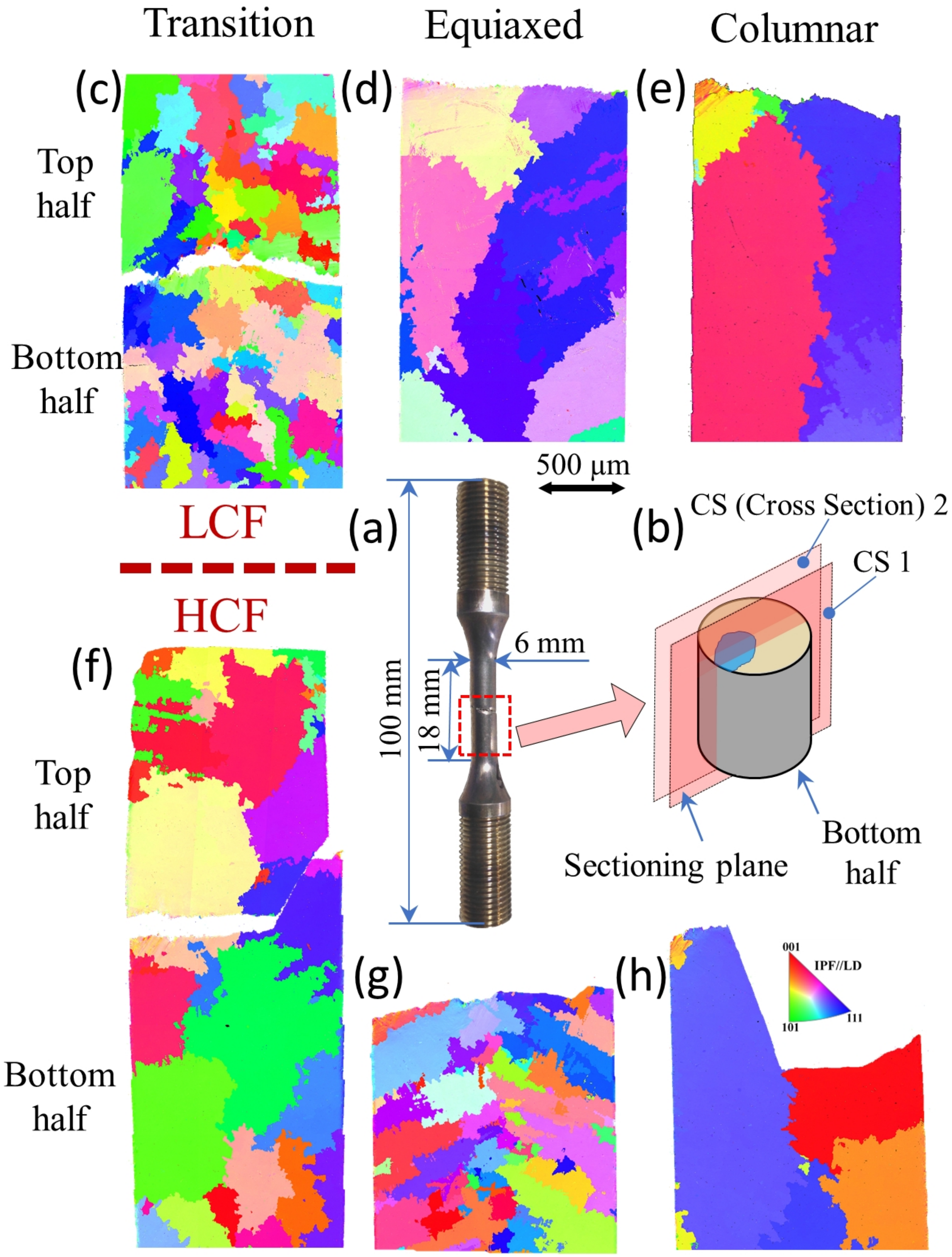
Transition
Equiaxed
Columnar
(c)
(d)
(e)
Top half
Bottom half
500 µm
(a)
(b)
CS (Cross Section) 2
CS 1
LCF
HCF
6 mm
18 mm
100 mm
Sectioning plane
Bottom half
(f)
Top half
Bottom half
(g)
(h)
001
IPF//LD
101
111

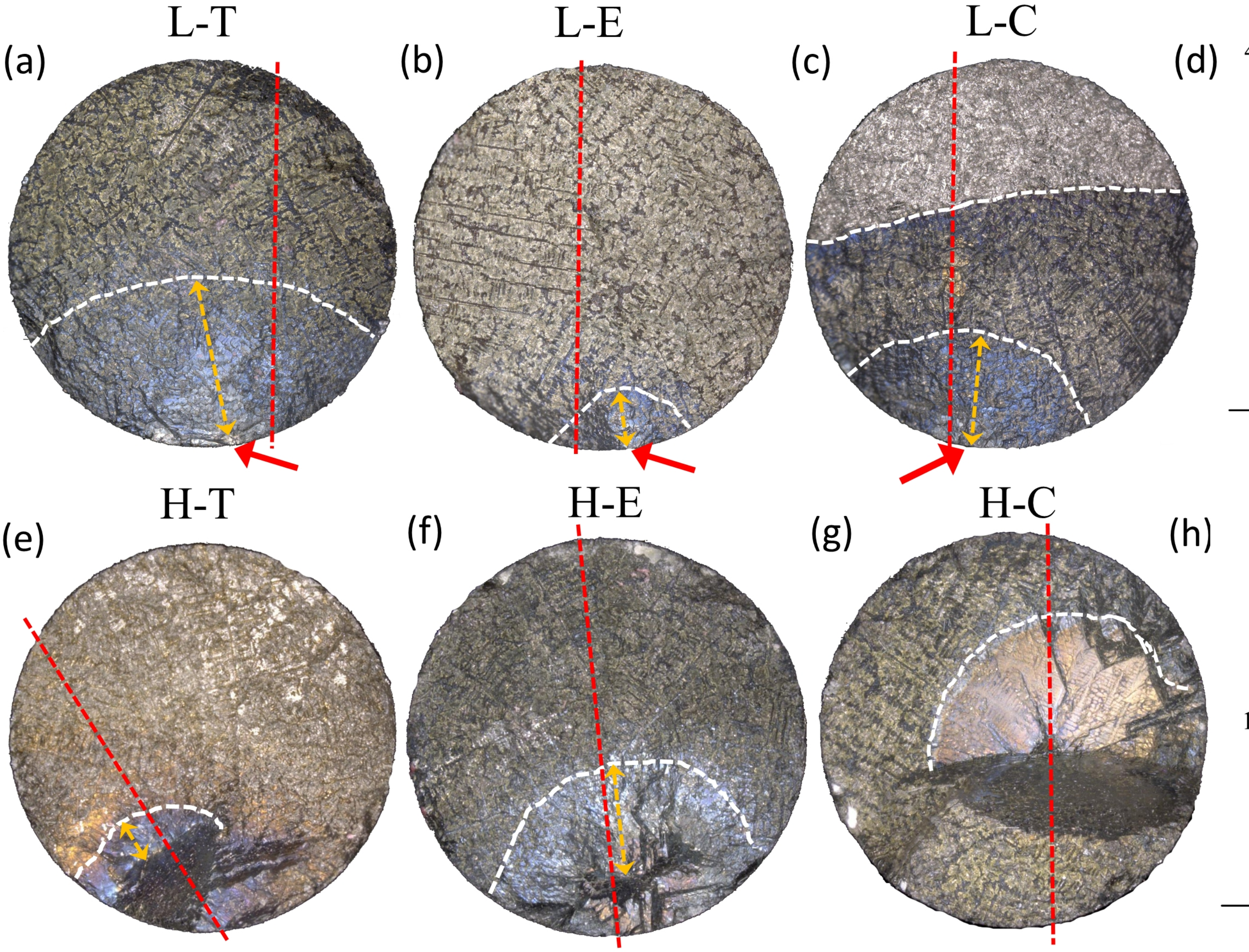
L-T
L-E
L-C
(a)
(b)
(c)
(d)
H-T
H-E
H-C
(e)
(f)
(g)
(h)

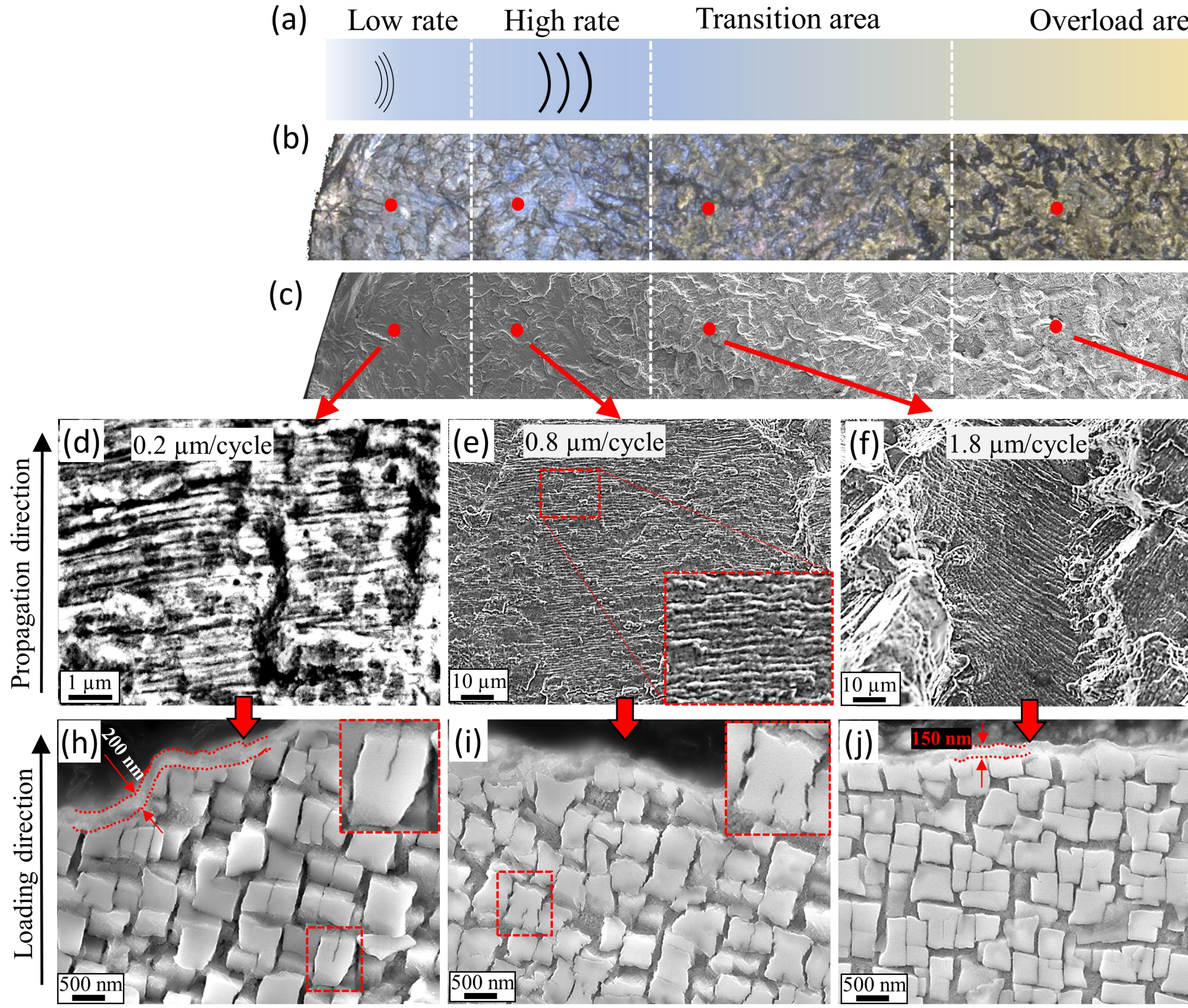
(a)
Low rate
High rate
Transition area
Overload are
(b)
(c)
Propagation direction
(d)
0.2 µm/cycle
1 µm
(e)
0.8 µm/cycle
10 µm
(f)
1.8 µm/cycle
10 µm
Loading direction
(h)
200 nm
500 nm
(i)
500 nm
(j)
150 nm
500 nm

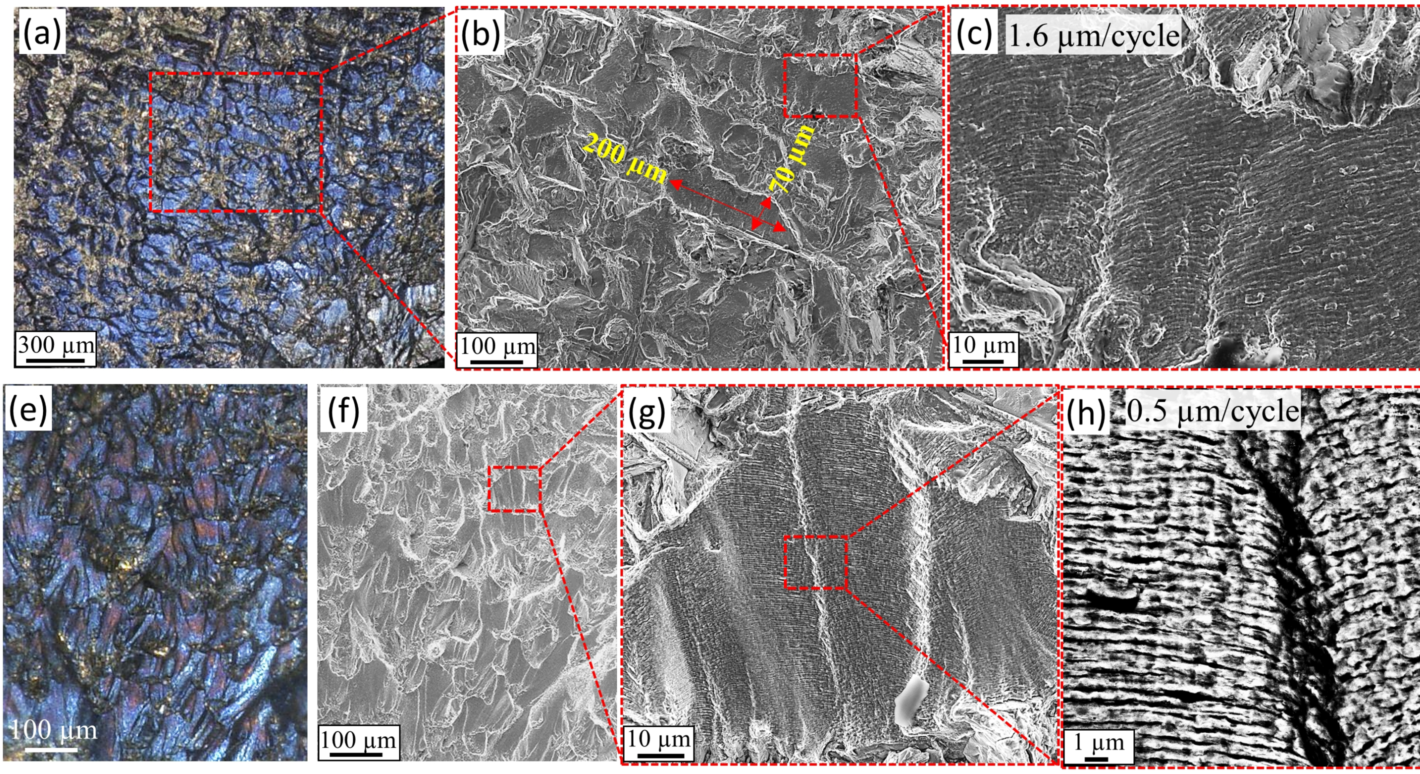
(a)
300 μm
(b)
200 μm
70 μm
100 μm
(c)
1.6 μm/cycle
10 μm
(e)
100 μm
(f)
100 μm
(g)
10 μm
(h)
0.5 μm/cycle
1 μm

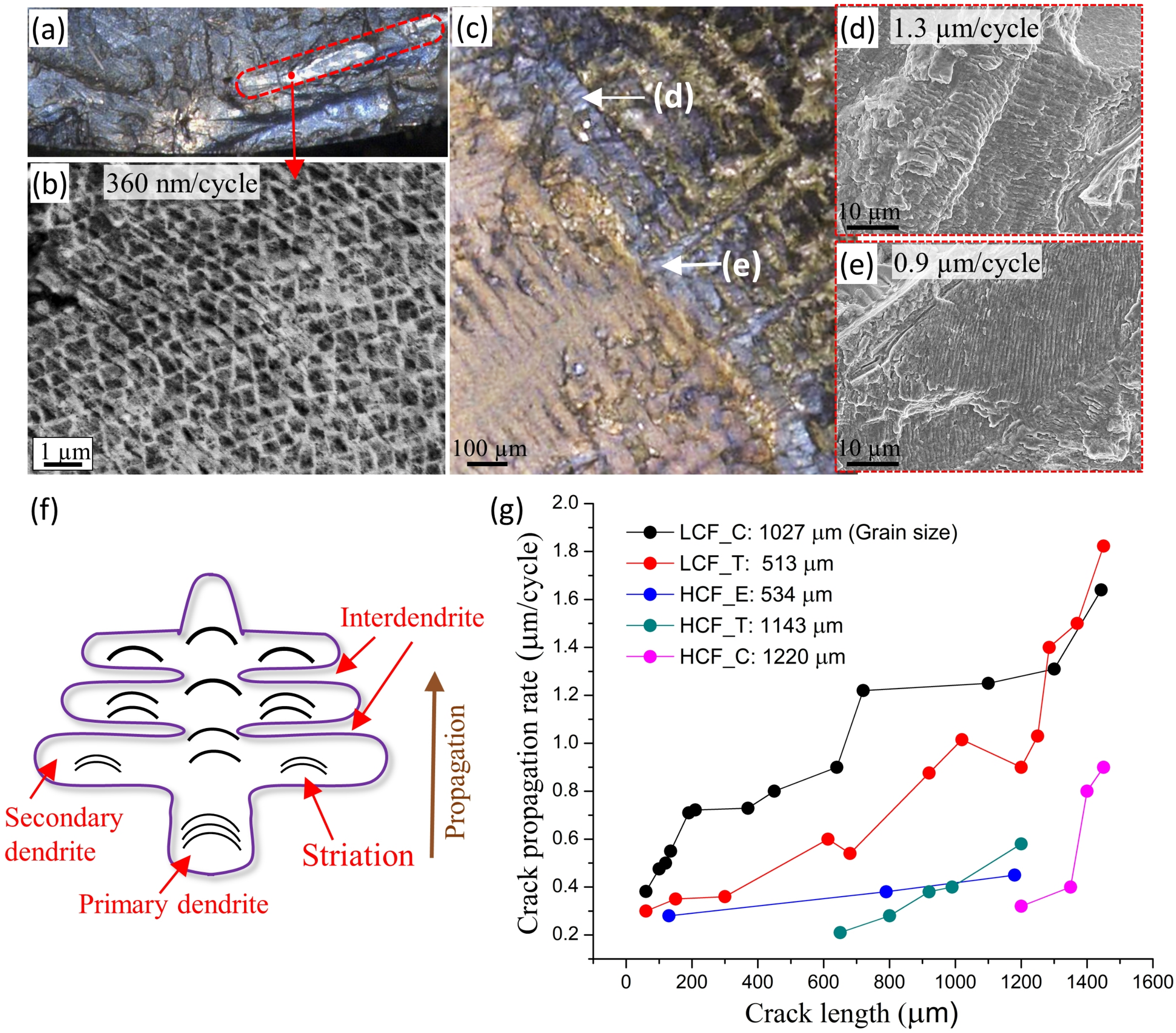
(a)
(b)
360 nm/cycle
1 μm
(c)
(d)
(e)
100 μm
(d)
1.3 μm/cycle
10 μm
(e)
0.9 μm/cycle
10 μm
(f)
Interdendrite
Propagation
Secondary dendrite
Striation
Primary dendrite
(g)
LCF_C: 1027 μm (Grain size)
LCF_T: 513 μm
HCF_E: 534 μm
HCF_T: 1143 μm
HCF_C: 1220 μm
Crack propagation rate (μm/cycle)
0.2
0.4
0.6
0.8
1.0
1.2
1.4
1.6
1.8
2.0
Crack length (μm)
0
200
400
600
800
1000
1200
1400
1600

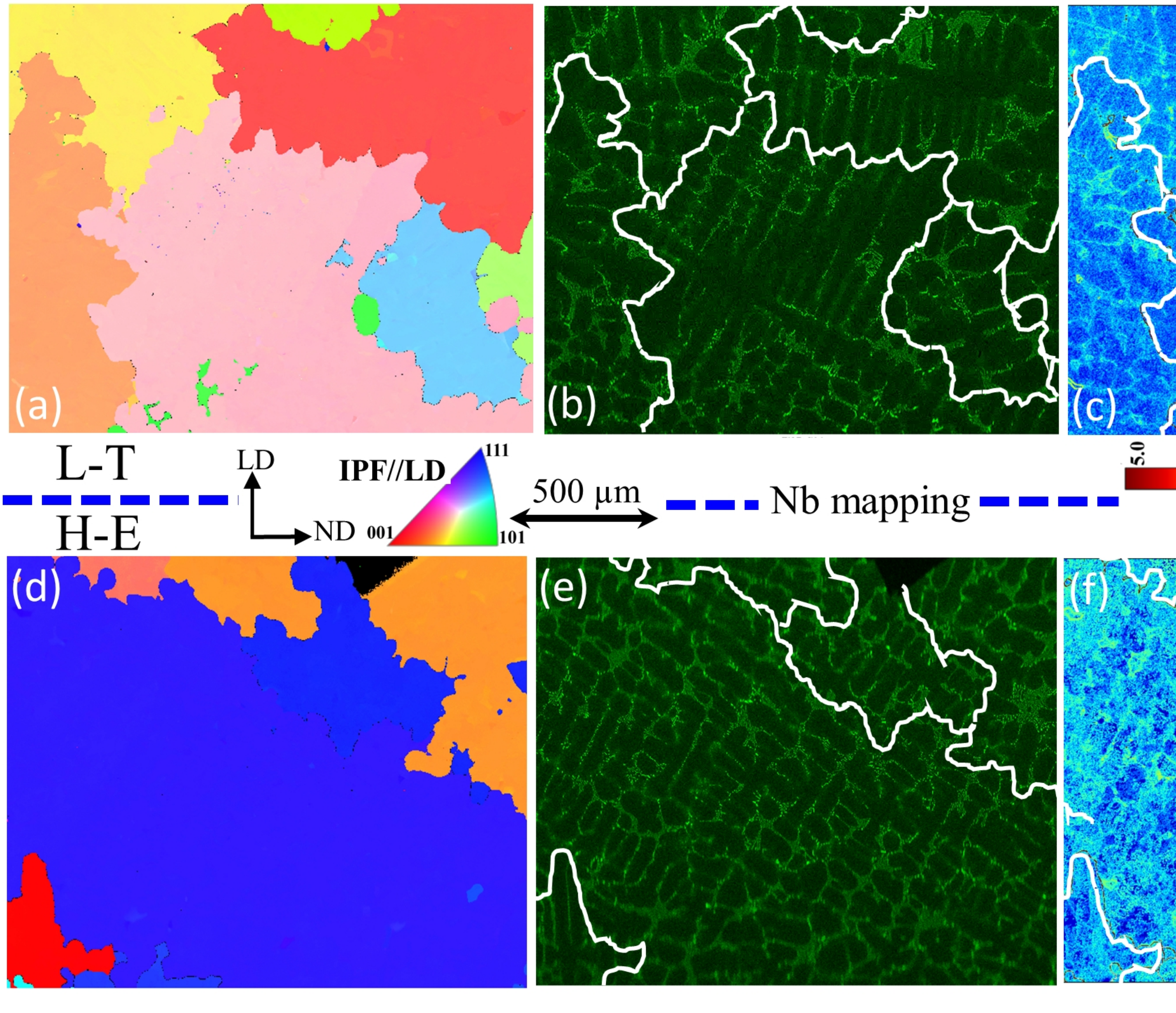
(a)
(b)
(c)
L-T
H-E
LD
ND
IPF//LD
111
001
101
500 μm
Nb mapping
5.0
(d)
(e)
(f)

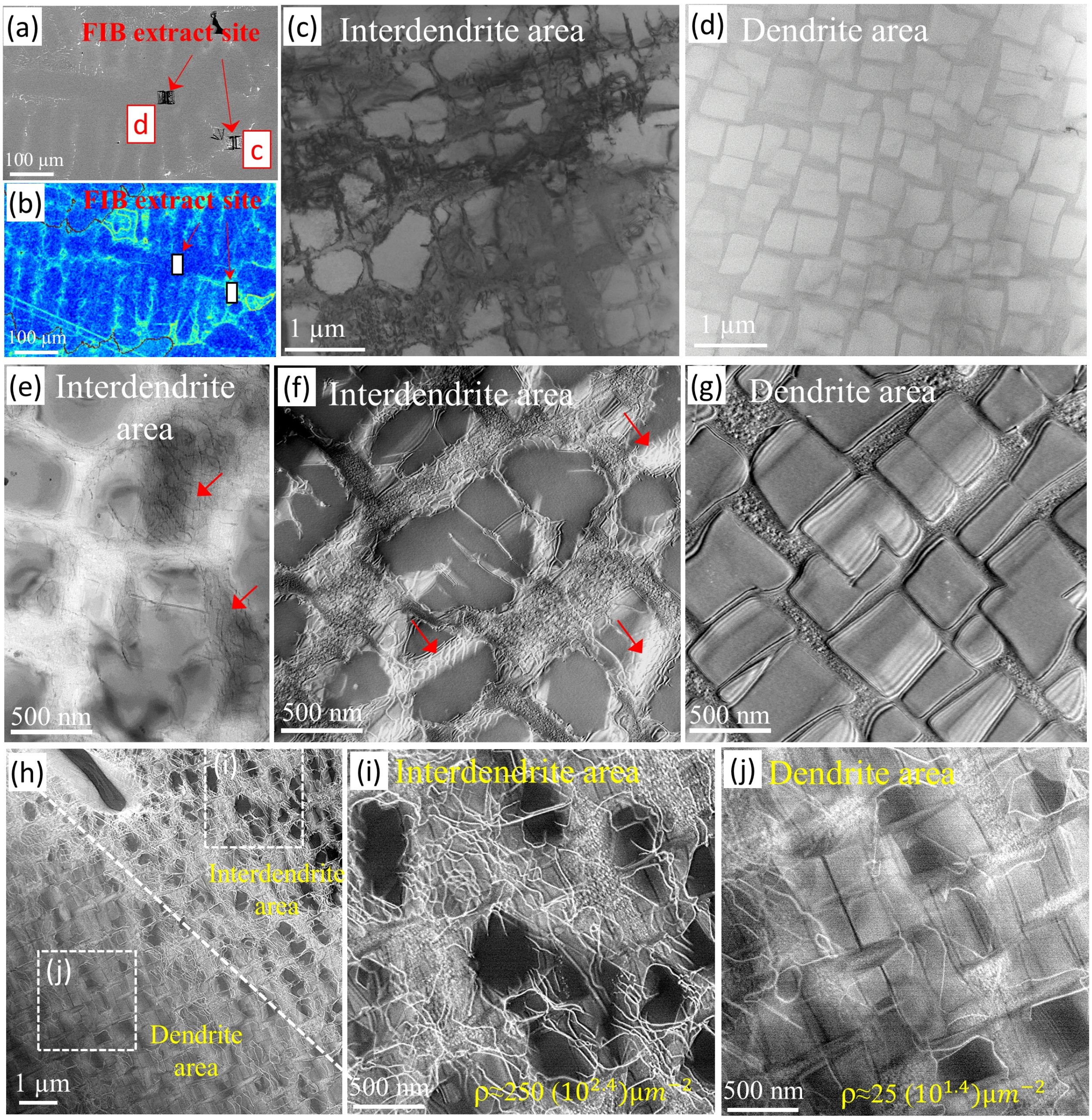
(a)
FIB extract site
d
c
100 μm
(b)
FIB extract site
100 μm
(c) Interdendrite area
1 μm
(d) Dendrite area
1 μm
(e) Interdendrite area
500 nm
(f) Interdendrite area
500 nm
(g) Dendrite area
500 nm
(h)
(i)
Interdendrite area
(j)
Dendrite area
1 μm
(i) Interdendrite area
500 nm
$\rho\approx250\ (10^{2.4})\mu m^{-2}$
(j) Dendrite area
500 nm
$\rho\approx25\ (10^{1.4})\mu m^{-2}$

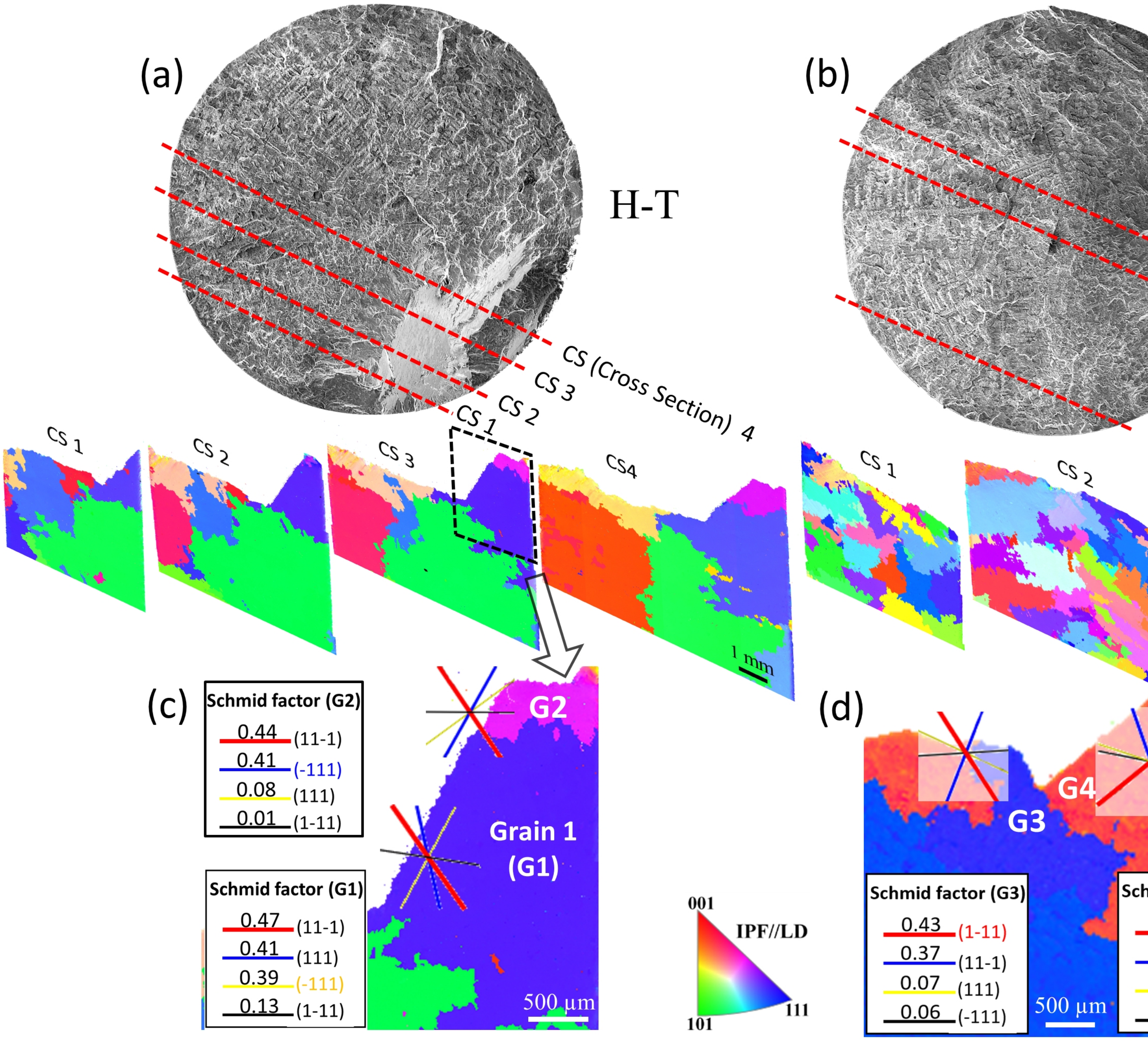
(a)
H-T
CS (Cross Section) 4
CS 3
CS 2
CS 1
CS 1
CS 2
CS 3
CS4
1 mm
(b)
CS 1
CS 2
(c)
Schmid factor (G2)
0.44 (11-1)
0.41 (-111)
0.08 (111)
0.01 (1-11)
G2
Grain 1 (G1)
Schmid factor (G1)
0.47 (11-1)
0.41 (111)
0.39 (-111)
0.13 (1-11)
500 μm
001
IPF//LD
101
111
(d)
G4
G3
Schmid factor (G3)
0.43 (1-11)
0.37 (11-1)
0.07 (111)
0.06 (-111)
500 μm
Sch

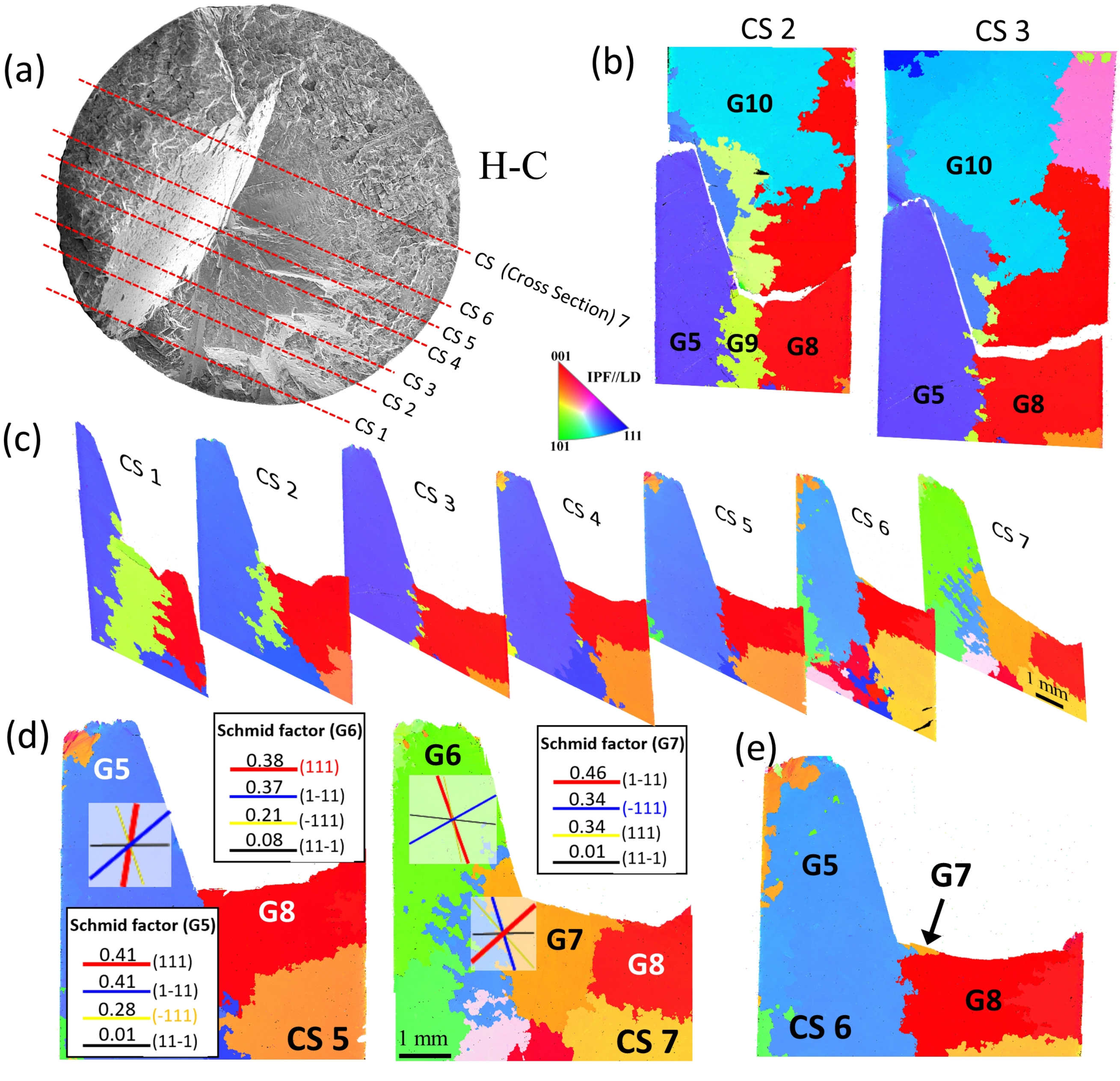
(a)
H-C
CS (Cross Section) 7
CS 6
CS 5
CS 4
CS 3
CS 2
CS 1
(b)
CS 2
CS 3
G10
G10
G5
G9
G8
G5
G8
001
IPF//LD
101
111
(c)
CS 1
CS 2
CS 3
CS 4
CS 5
CS 6
CS 7
1 mm
(d)
G5
Schmid factor (G6)
0.38 (111)
0.37 (1-11)
0.21 (-111)
0.08 (11-1)
G8
Schmid factor (G5)
0.41 (111)
0.41 (1-11)
0.28 (-111)
0.01 (11-1)
CS 5
G6
Schmid factor (G7)
0.46 (1-11)
0.34 (-111)
0.34 (111)
0.01 (11-1)
G7
G8
1 mm
CS 7
(e)
G5
G7
G8
CS 6

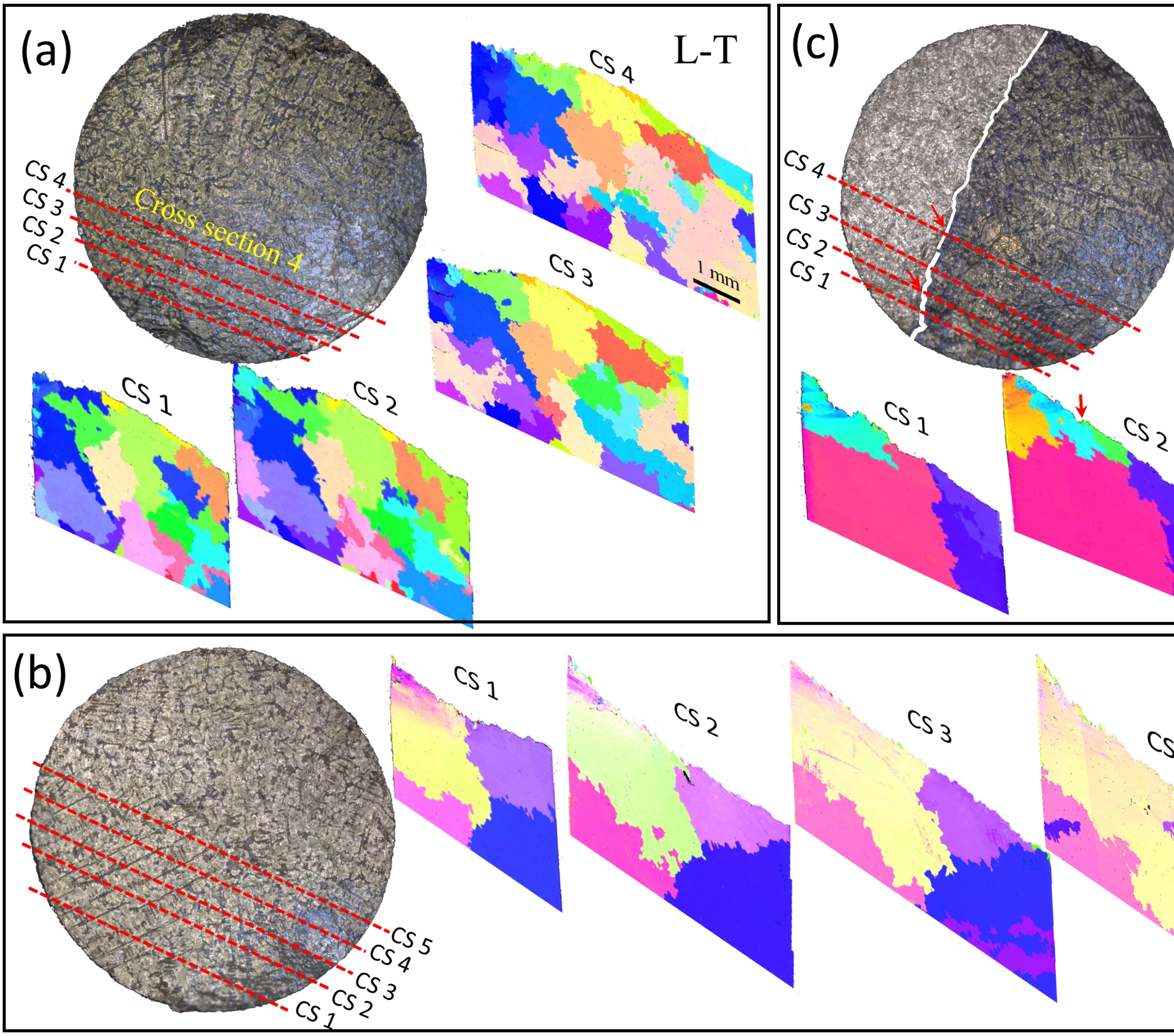
(a)
L-T
CS 4
CS 3
CS 2
CS 1
Cross section 4
CS 4
1 mm
CS 3
CS 1
CS 2
(c)
CS 4
CS 3
CS 2
CS 1
CS 1
CS 2
(b)
CS 1
CS 2
CS 3
CS 5
CS 4
CS 3
CS 2
CS 1

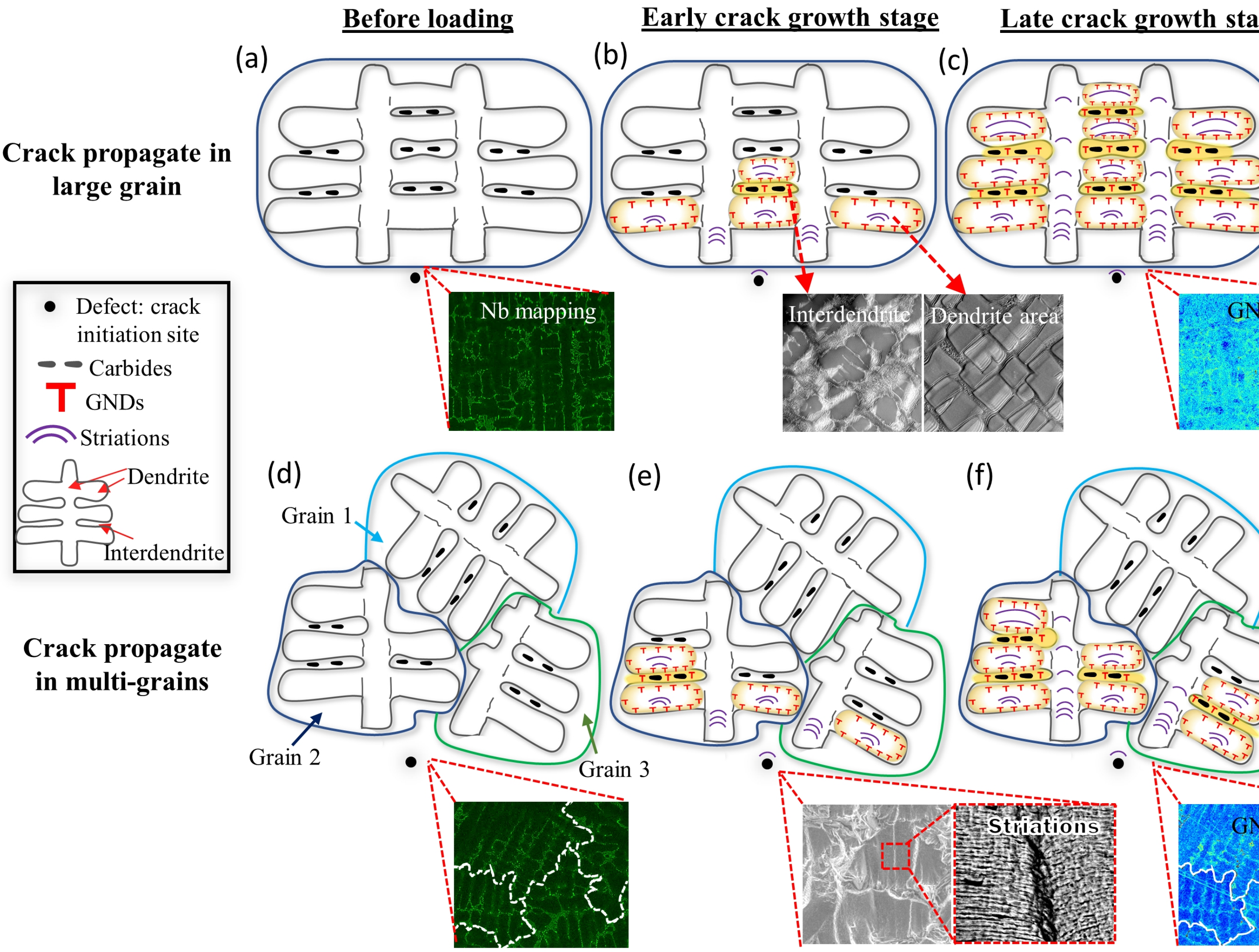
Before loading
Early crack growth stage
Late crack growth sta
(a)
(b)
(c)
Crack propagate in large grain
Nb mapping
Interdendrite
Dendrite area
GN
Defect: crack initiation site
Carbides
GNDs
Striations
Dendrite
Interdendrite
(d)
(e)
(f)
Grain 1
Grain 2
Grain 3
Crack propagate in multi-grains
Striations
GN

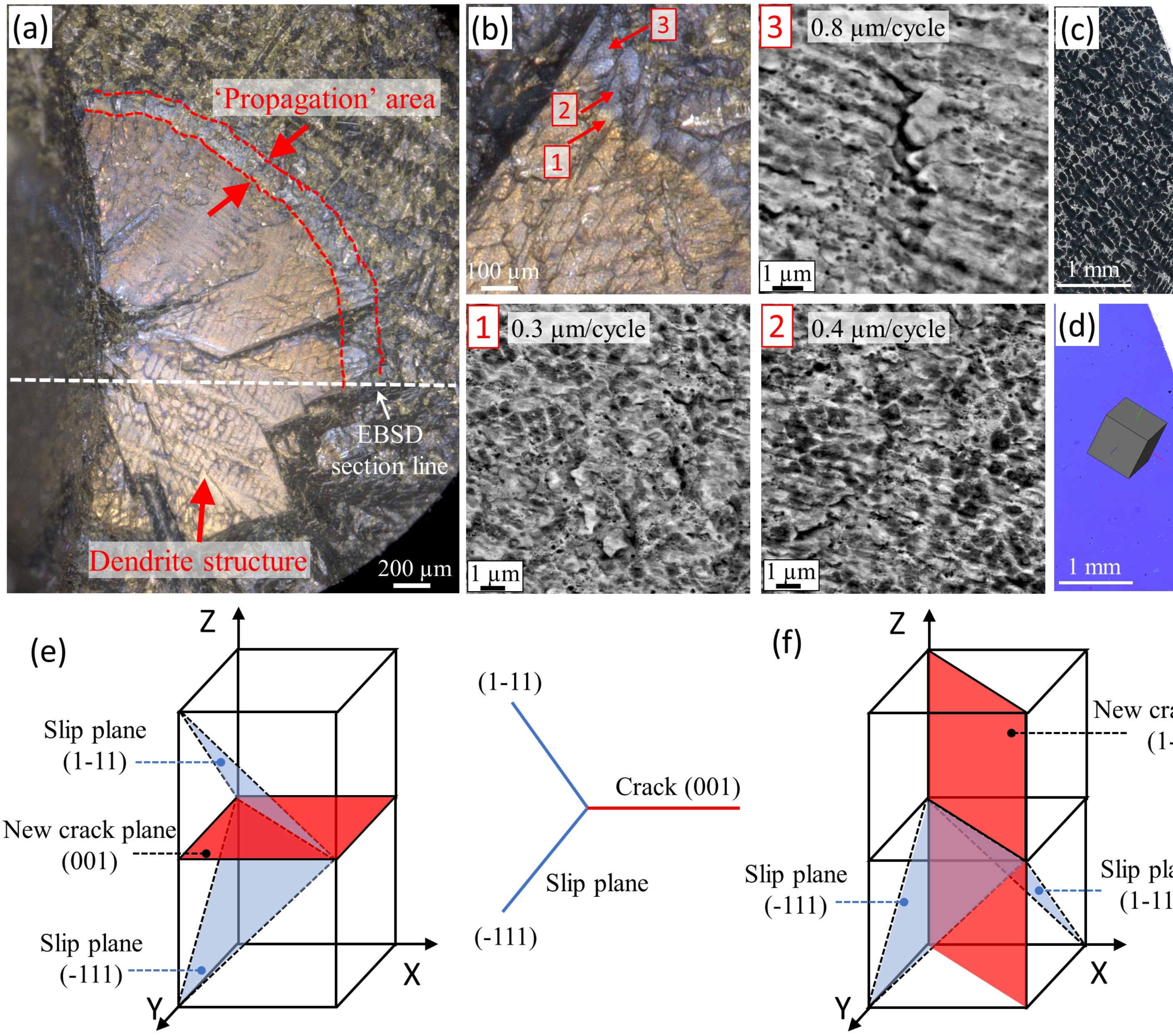
(a)
'Propagation' area
EBSD section line
Dendrite structure
200 μm
(b)
3
2
1
100 μm
3 0.8 μm/cycle
1 μm
(c)
1 mm
1 0.3 μm/cycle
1 μm
2 0.4 μm/cycle
1 μm
(d)
1 mm
(e)
Z
X
Y
Slip plane (1-11)
New crack plane (001)
Slip plane (-111)
(1-11)
Crack (001)
Slip plane
(-111)
(f)
Z
X
Y
New cra
(1-
Slip plane (-111)
Slip pla
(1-11

Table 1 IN731C chemical composition (w

Ni	Cr	Al	Mo	Nb+Ta	Ti	C
Bal	12.50	6.10	4.20	2.20	0.80	0.12

Declarations of interest: None

Supplementary Material

The Effects of Grain Size, Dendritic Structure and Crystallographic Orientation on Fatigue Crack Propagation in IN713C Nickel-Based Superalloy

G. Liu[1]*, S. Winwood[2], K. Rhodes[2], S. Birosca[1]*

[1] Materials Research Centre, College of Engineering, Swansea University, Bay Campus, Swansea SA1 8EN, UK.

[2] Cummins Turbo Technologies, St. Andrews Rd., Huddersfield HD1 6RA, UK.

Corresponding author:

E-mail address: Gang.Liu@swansea.ac.uk (G.Liu); S.Birosca@swansea.ac.uk (S.Birosca)

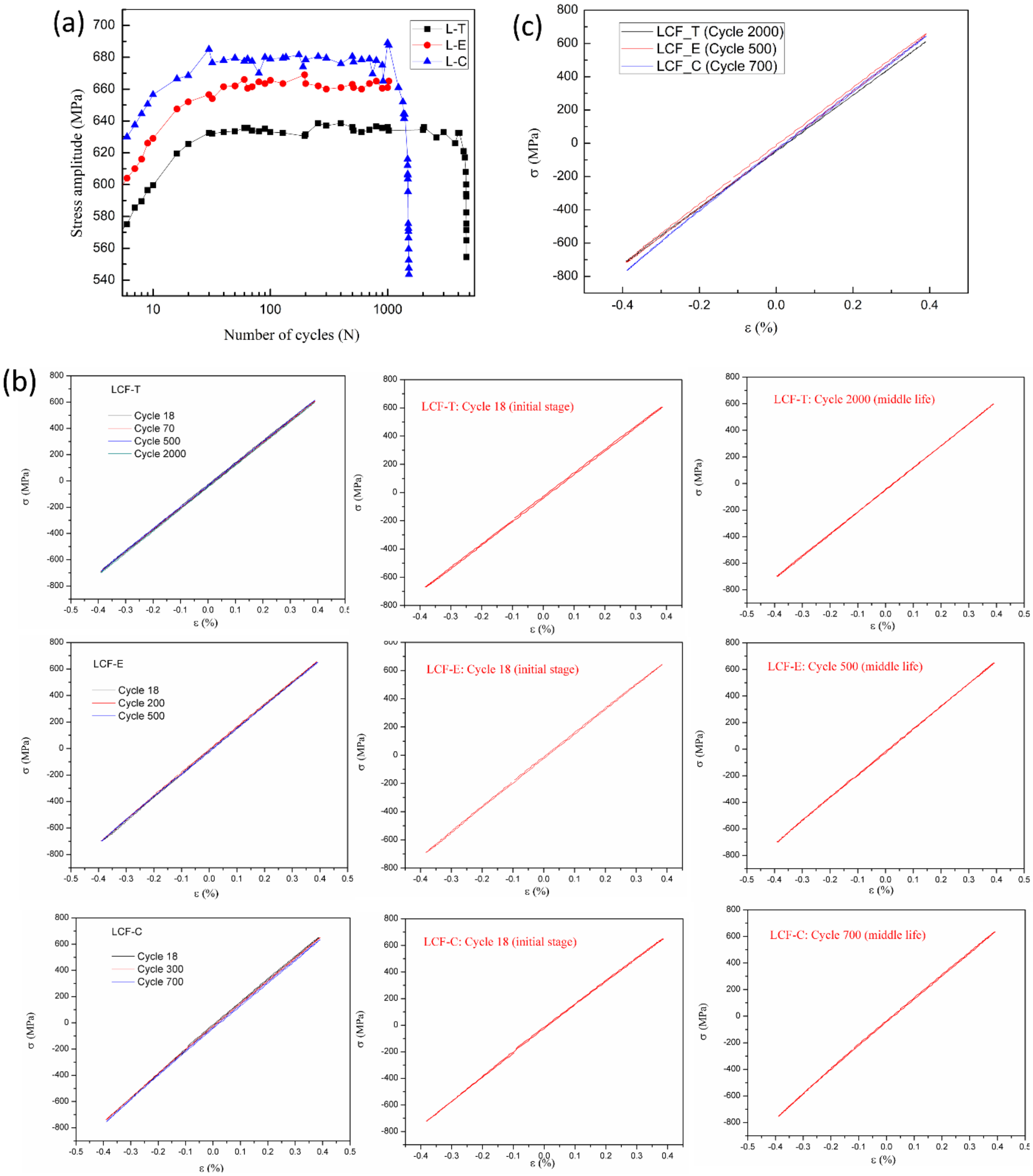

Supplementary Fig. 1 (a) The stress amplitude of selected cycles in LCF tests. (b) LCF stress-strain loop figure in specific cycles in each sample. (c) Stress-strain loop of specific cycle in LCF samples.

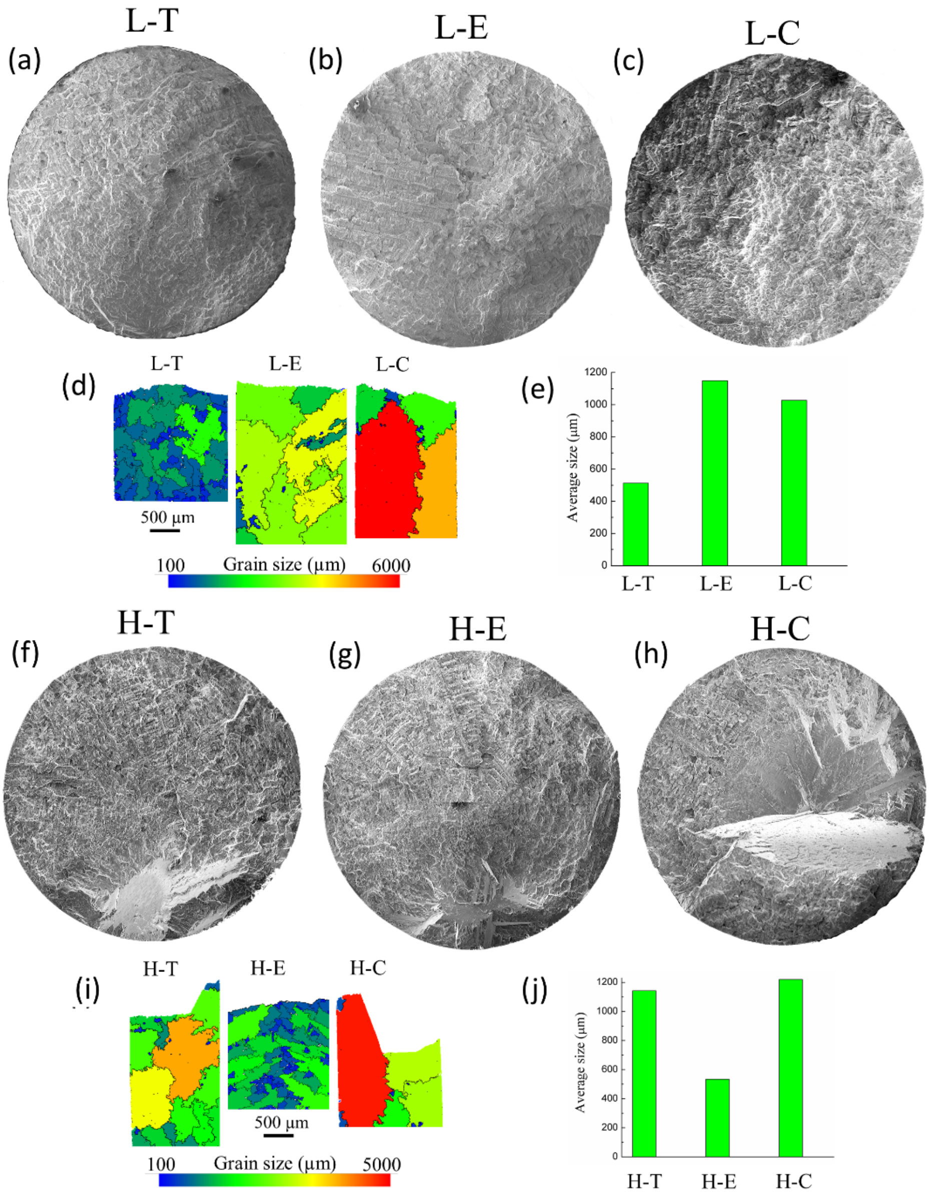

Supplementary Fig. 2 SEM images of fracture surface in LCF (a-c) and HCF (d-f) samples. Imaging position are as same as in Fig. 4. (d-e) and (i-j) grain size in LCF and HCF samples.

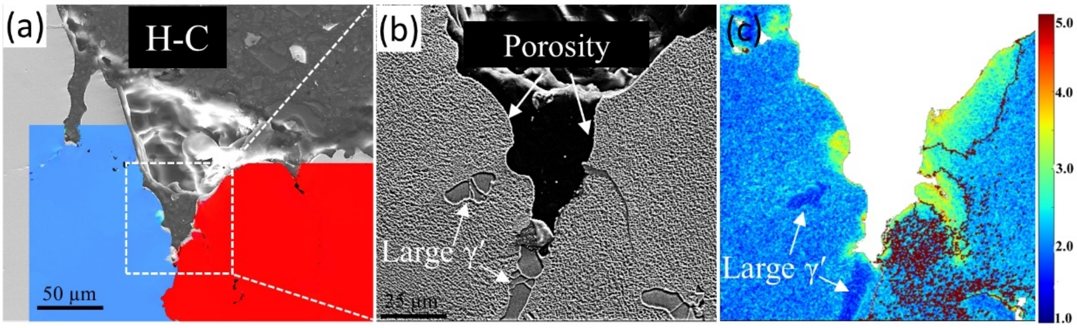

Supplementary Fig. 3 Cross section of pores. (a-c) Pore of initiation site in H-C, sectioning line is shown in Fig.5i with red dashed line, (b) The magnified area of white box area in (a), and (c) GND map of (b). IPF are superimposed on scanning surface in (a). Step size for GND mapping is 200 nm.

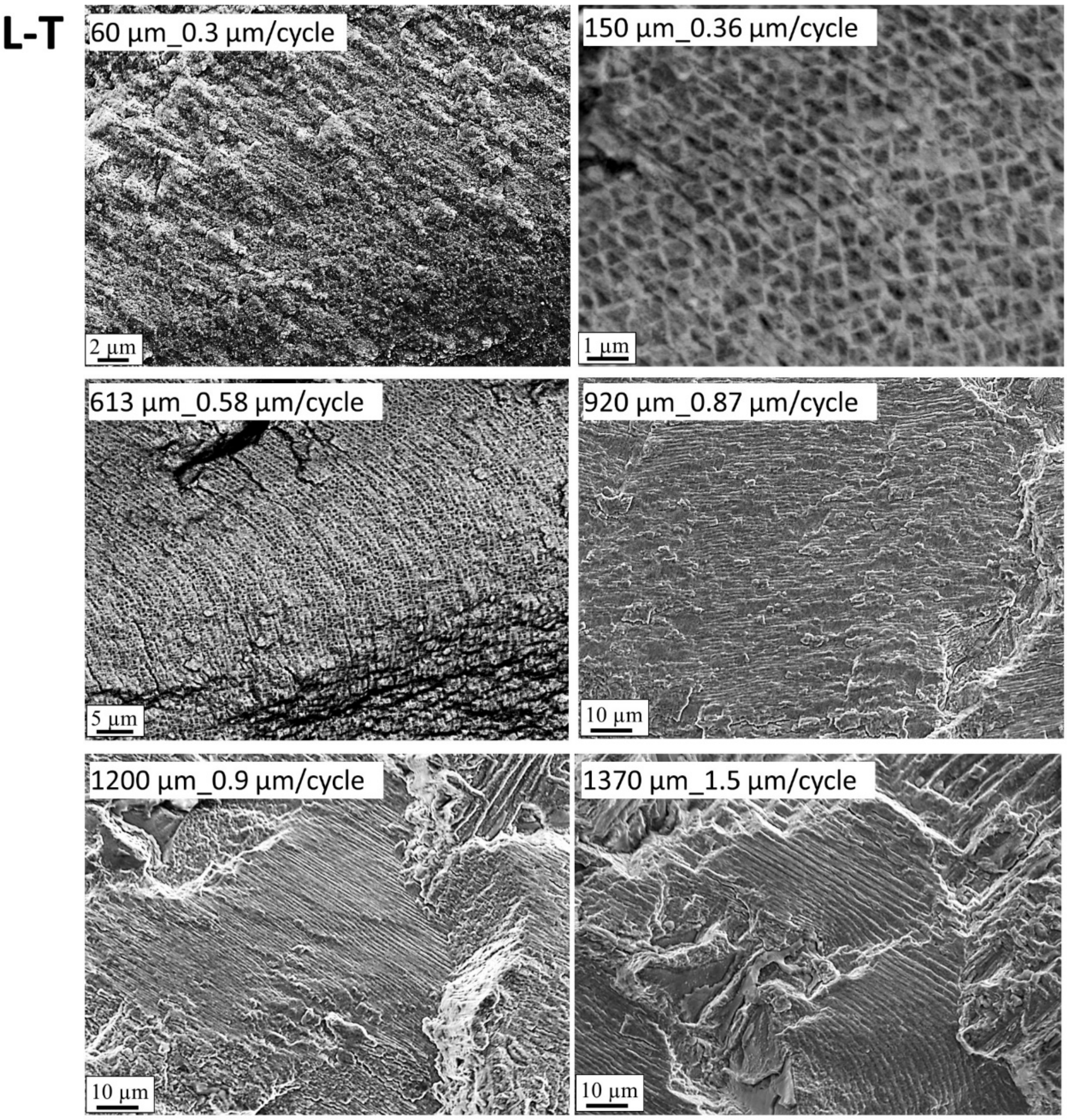
L-T
60 µm_0.3 µm/cycle
2 µm
150 µm_0.36 µm/cycle
1 µm
613 µm_0.58 µm/cycle
5 µm
920 µm_0.87 µm/cycle
10 µm
1200 µm_0.9 µm/cycle
10 µm
1370 µm_1.5 µm/cycle
10 µm

L-C

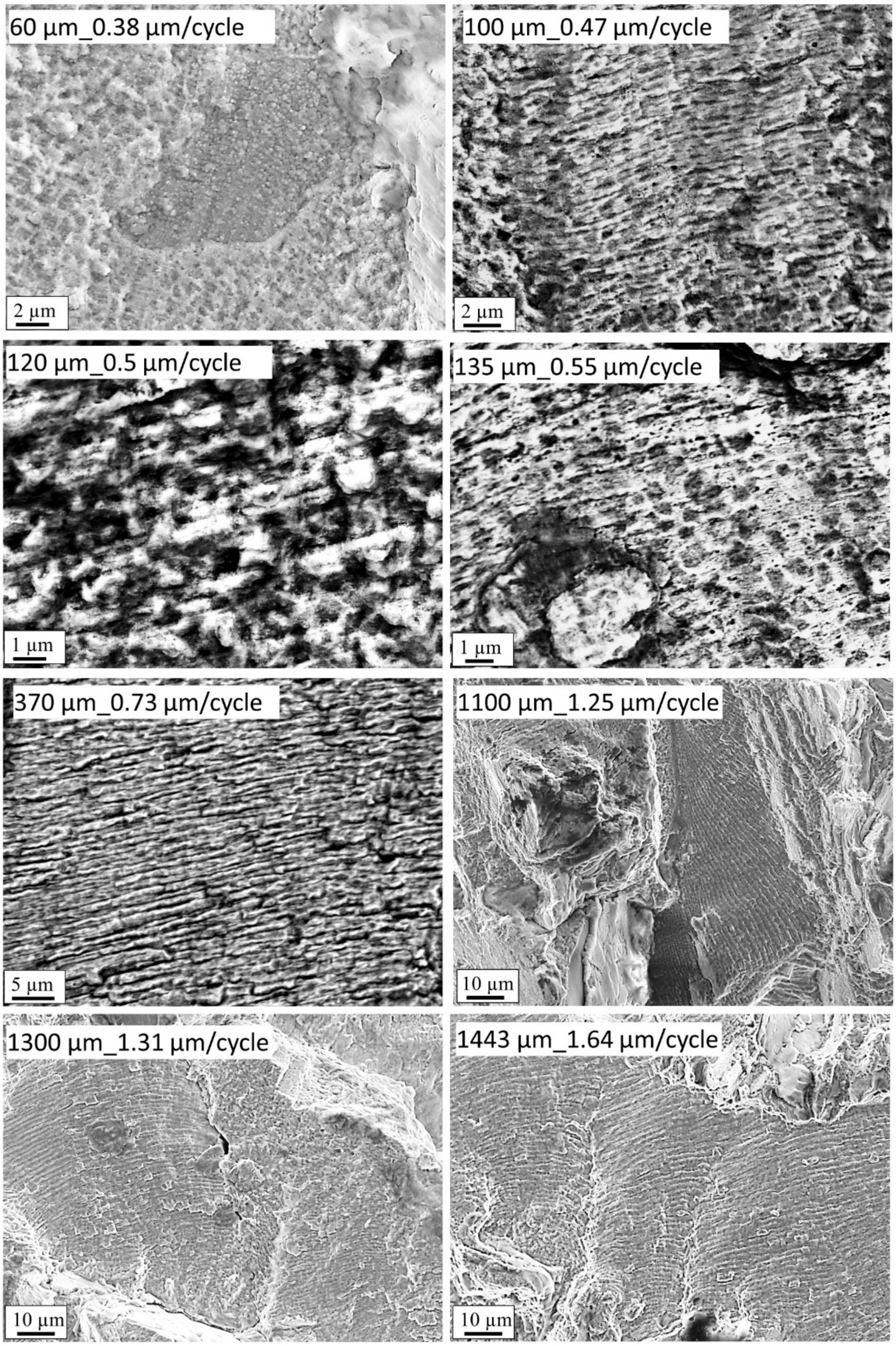
60 µm_0.38 µm/cycle
2 µm
100 µm_0.47 µm/cycle
2 µm
120 µm_0.5 µm/cycle
1 µm
135 µm_0.55 µm/cycle
1 µm
370 µm_0.73 µm/cycle
5 µm
1100 µm_1.25 µm/cycle
10 µm
1300 µm_1.31 µm/cycle
10 µm
1443 µm_1.64 µm/cycle
10 µm

H-T

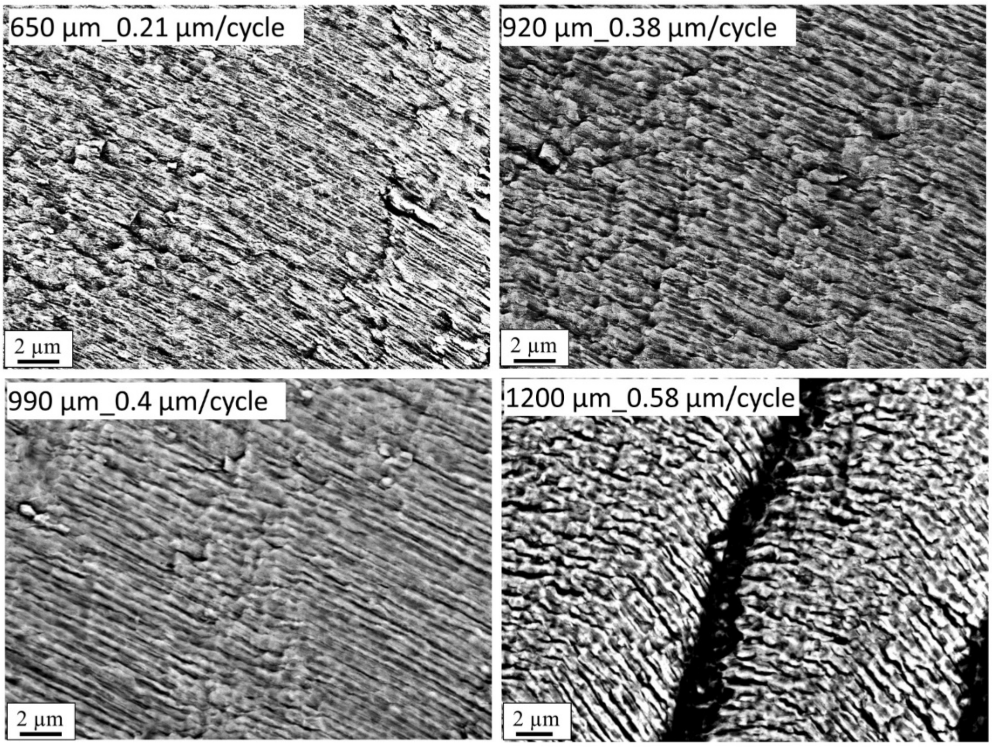
650 µm_0.21 µm/cycle
2 µm
920 µm_0.38 µm/cycle
2 µm
990 µm_0.4 µm/cycle
2 µm
1200 µm_0.58 µm/cycle
2 µm

H-E

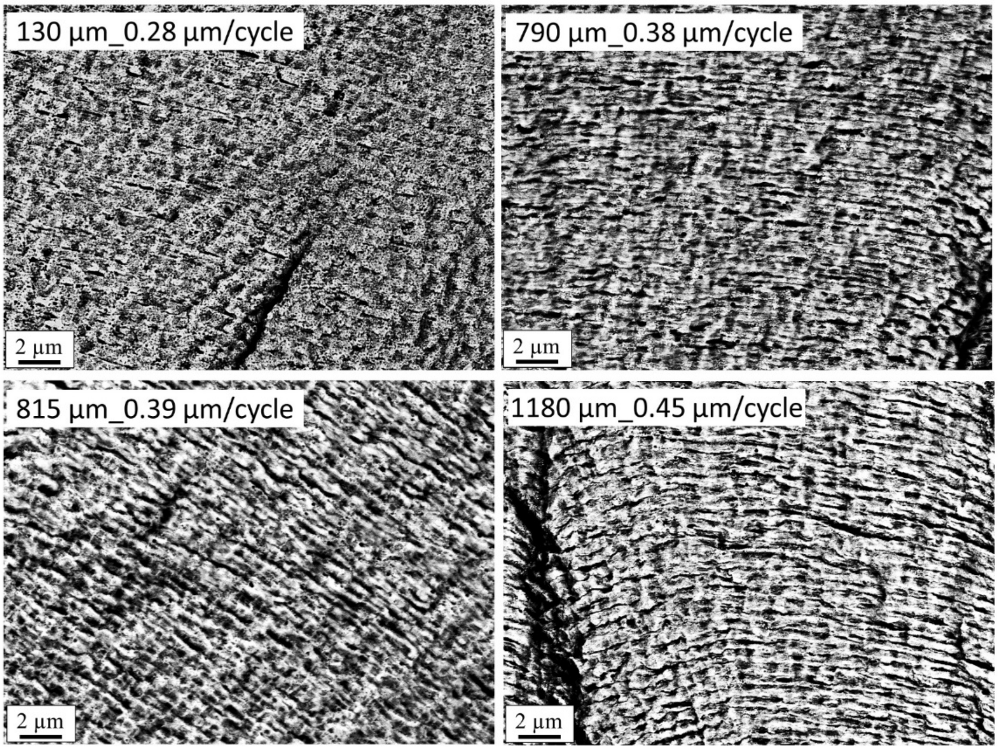
130 µm_0.28 µm/cycle
2 µm
790 µm_0.38 µm/cycle
2 µm
815 µm_0.39 µm/cycle
2 µm
1180 µm_0.45 µm/cycle
2 µm

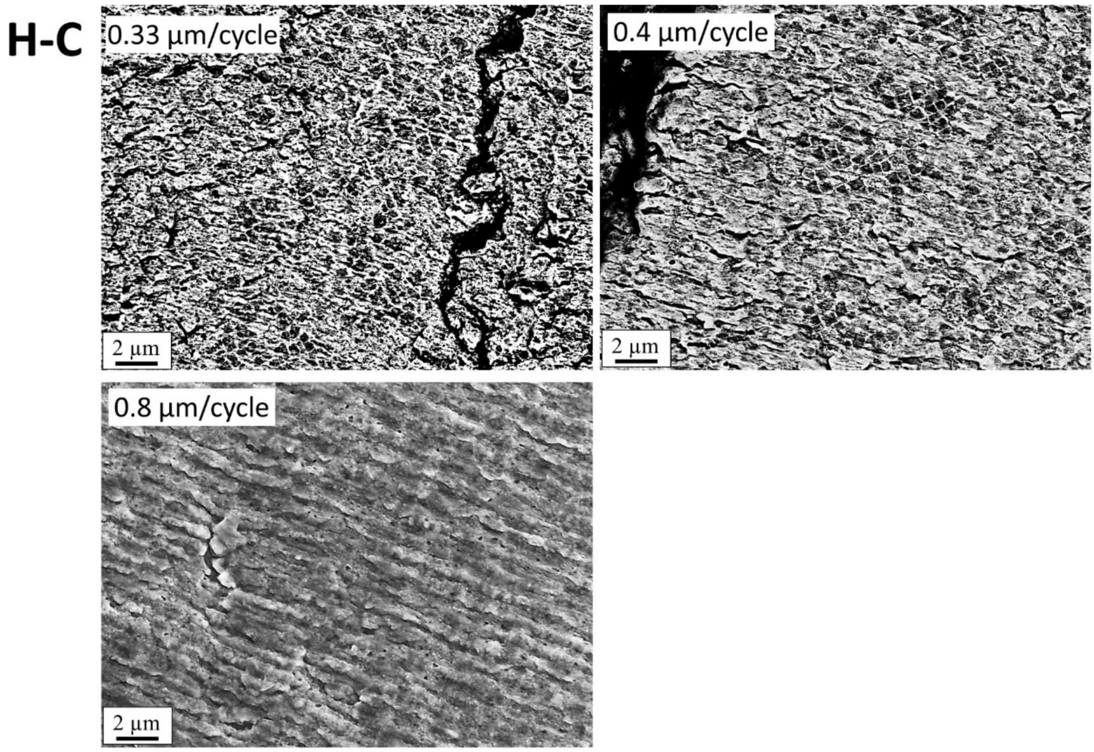

Supplementary Fig. 4 Examples of striation spacing measurement and crack propagation rate determination in sample L-T, L-C, H-T, H-E and H-C. Crack length (or distance from the crack initiation point, first value) and crack propagation rate (second value) for each site are shown in each figure. There is no distance value in H-C sample because of the large brittle cracking area from initiation site in this case. They are part of the data point in drawing the Fig. 7g in the text.

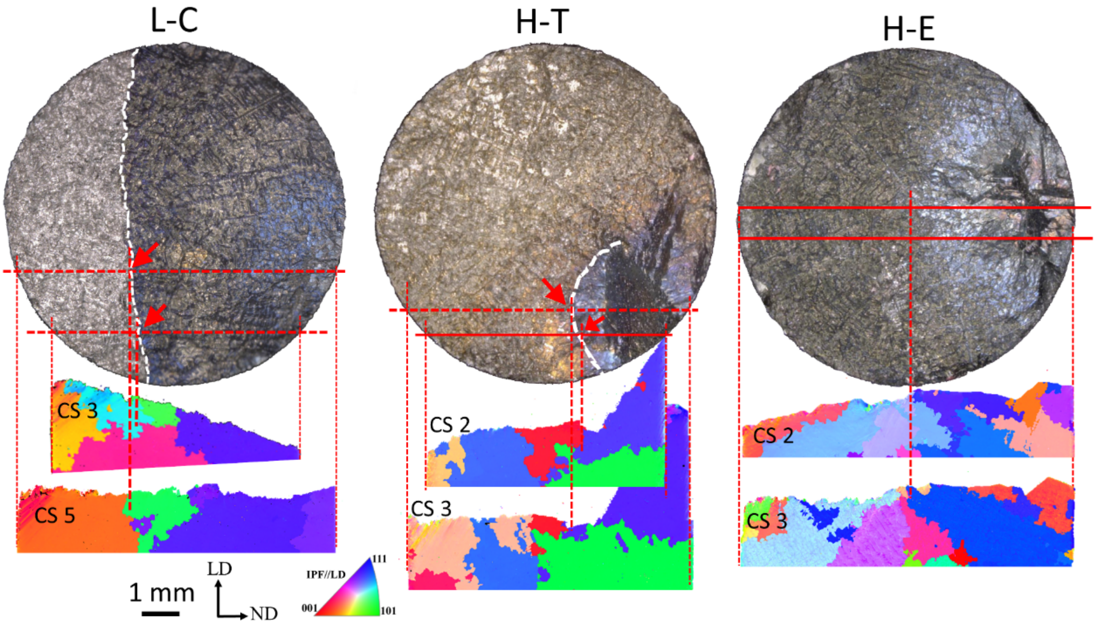

Supplementary Fig. 5 The effect of grain boundary on the final stage of crack propagation. Examples are shown in L-C, H-T and H-E samples. The wthite dash lines indicate the transition from propagation to overload stage. Intersection points of these transition lines and cross section lines are indicated by red arrows, and also indicated in IPFs.